iScience

CellPress

Article

Highly Efficient Aggregation-Induced Electrochemiluminescence of Polyfluorene Derivative Nanoparticles Containing Tetraphenylethylene

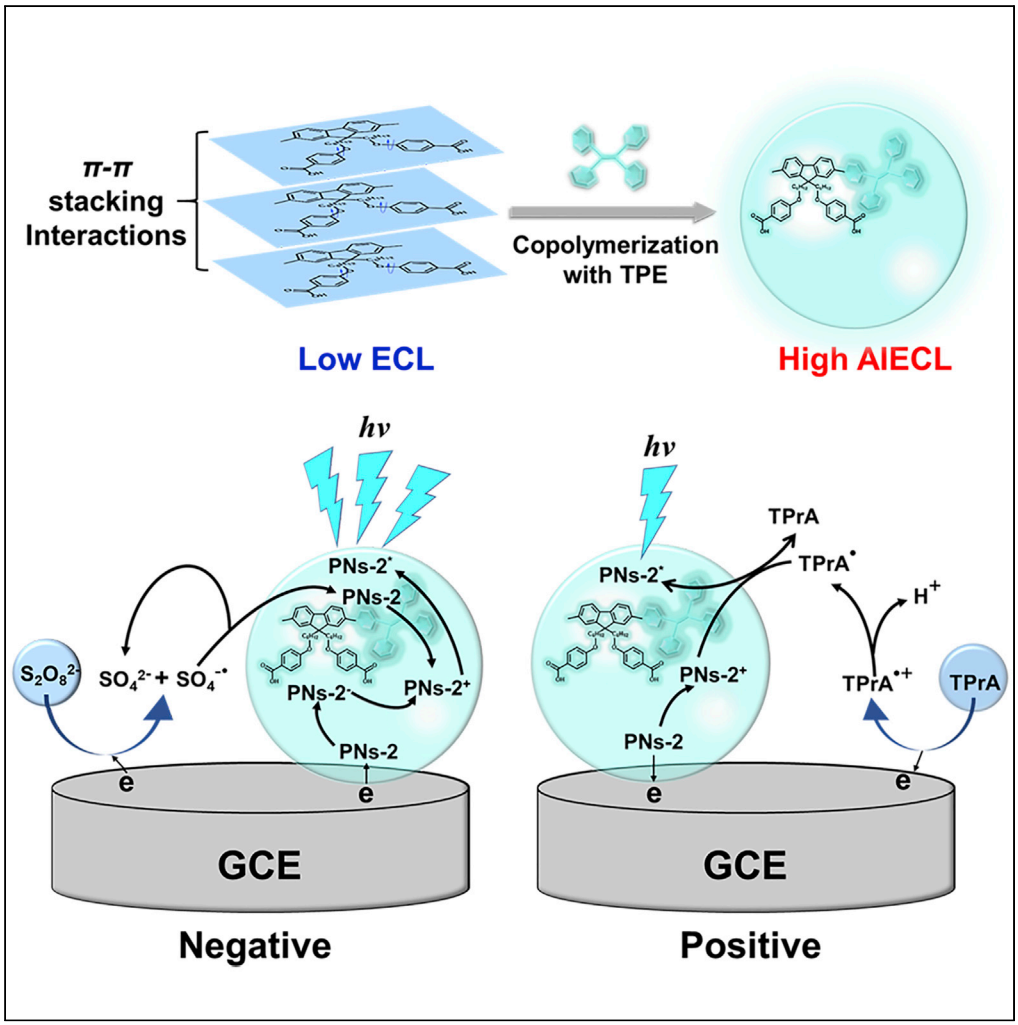

Si-Yuan Ji, Wei Zhao, Hang Gao, ..., Yi-Wu Quan, Jing-Juan Xu, Hong-Yuan Chen

chxu@nju.edu.cn (C.-H.X.)
quanyiwu@nju.edu.cn (Y.-W.Q.)
xujj@nju.edu.cn (J.-J.X.)

HIGHLIGHTS

AIECL of polyfluorene nanoparticles containing tetraphenylethylene is reported

TPE unit limits the stacking interactions of the molecular to enhance the ECL intensity

The ECL efficiency of copolymer nanoparticles is higher than that of $Ru(bpy)_3^{2+}$

Annihilation and co-reactant transient tests clarified the ECL generation mechanisms

Ji et al., iScience *23*, 100774
January 24, 2020
https://doi.org/10.1016/j.isci.2019.100774

iScience

CellPress

Article

Highly Efficient Aggregation-Induced Electrochemiluminescence of Polyfluorene Derivative Nanoparticles Containing Tetraphenylethylene

Si-Yuan Ji,[1,4] Wei Zhao,[1,4] Hang Gao,[2] Jian-Bin Pan,[1] Cong-Hui Xu,[1,*] Yi-Wu Quan,[3,*] Jing-Juan Xu,[1,5,*] and Hong-Yuan Chen[1]

SUMMARY

The aggregation-induced electrochemiluminescence (AIECL) of polyfluorene derivative nanoparticles containing tetraphenylethylene (TPE) in aqueous media is reported in this work. The TPE unit limits the intramolecular free rotation of phenyl rings, as well as the π-π stacking interactions of molecules, which significantly enhances ECL signal of the polyfluorene nanoparticles. With co-reactants of tri-n-propylamine (TPrA) and $S_2O_8^{2-}$, the copolymer nanoparticles show visualized ECL emissions at both positive and negative potentials. The ECL efficiency of copolymer nanoparticles in solid state is 163% compared with that of standard ECL species, $Ru(bpy)_3^{2+}$. And at negative potential, the ECL intensity of copolymer nanoparticles is even stronger with 6.5 times compared with that at positive potential. The ECL generation mechanisms are analyzed detailed by annihilation and co-reactant route transient ECL test (millisecond scale). This work provides a reference for the organic structure design for AIECL and shows promising potential in luminescent device and biological applications.

INTRODUCTION

A novel concept of aggregation-induced electrochemiluminescence (AIECL) was officially proposed by De Cola's team in 2017, which indicated aggregation-induced emission (AIE) was also present in ECL system and achieved significant ECL signal amplification from platinum (II) complex (Carrara et al., 2017). In this system, the changed HOMO and LUMO energies by self-assembly led to the generation of the ECL excited state. This discovery has opened up a new field of ECL research and enkindled research enthusiasm for seeking luminescent molecules with AIECL properties. Recently, iridium-based redox polymers have been reported with unusually intense luminescence under the aggregate state, which were significantly greater than the analogous ruthenium-based materials (Carrara et al., 2018; Gao et al., 2018). Our group first reported that the carborane structure could enhance the ECL signal of carbazole molecule and established the relation between AIE organic structures and ECL properties (Wei et al., 2019a, 2019b). So far, research on AIECL is still in its infancy, focusing on the discovery of new molecules with AIECL properties (Han et al., 2019; Wei et al., 2019a, 2019b; Jiang et al., 2019a, 2019b). It is urgent to develop the ultra-efficient biocompatible AIECL luminophores with strong potential for biological applications (Valenti et al., 2017; Voci et al., 2018; Zhang et al., 2019).

Polyfluorene is a promising semiconductor π-conjugated polymer with high photoluminescence (PL) efficiency and good chemical stability (Scherf and List, 2002; Knaapila and Monkman, 2013; O'Carroll et al., 2008). Meanwhile the effective overlap of π orbitals of fluorene provides electronic coupling to promote electron and hole transfer (Josh et al., 2010; Qi et al., 2012; Voityuk, 2010), indicating that it is also a potential ECL emitter with the high efficiency. The electrochemistry and ECL properties of polyfluorene and its derivatives in organic solution have been reported in previous studies, and further works have been made to prepare aqueous phase dispersed polyfluorene nanoparticles (PNs) (Wong et al., 2002; Honmou et al., 2014; Chang et al., 2008). However, to our knowledge, the ECL efficiencies of all PNs reported were much lower than ruthenium and iridium complexes, mainly due to the aggregation quenching caused by the π-π stacking interactions of molecules (Omer et al., 2011; Suk et al., 2011a, 2011b), which seriously limited the wide application of PNs in aqueous phase ECL systems (Guo et al., 2018; Deng and Ju, 2013).

Here, we synthesized the polyfluorene derivative by copolymerization of fluorene with tetraphenylethylene (TPE), and the prepared copolymer nanoparticles exhibited strong aggregation-induced ECL in aqueous

[1]State Key Laboratory of Analytical Chemistry for Life Science, School of Chemistry and Chemical Engineering, Nanjing University, Nanjing 210023, China

[2]Key Lab of Mesoscopic Chemistry of MOE and Jiangsu Key Laboratory of Advanced Organic Materials, School of Chemistry and Chemical Engineering, Nanjing University, Nanjing 210023, China

[3]Key Laboratory of High Performance Polymer Materials & Technology of Ministry of Education, School of Chemistry and Chemical Engineering, Nanjing University, Nanjing 210023, China

[4]These authors contributed equally

[5]Lead Contact

*Correspondence: chxu@nju.edu.cn (C.-H.X.), quanyiwu@nju.edu.cn (Y.-W.Q.), xujj@nju.edu.cn (J.-J.X.)

https://doi.org/10.1016/j.isci.2019.100774

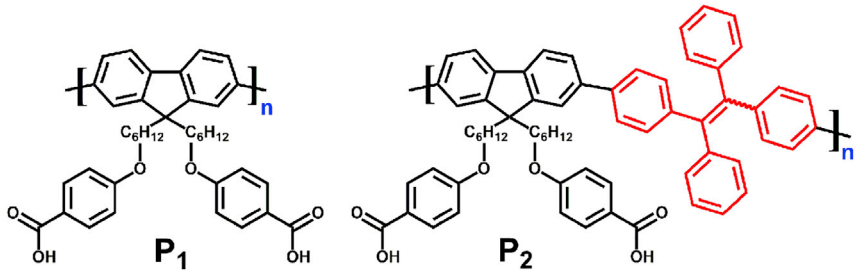

Scheme 1. Chemical Structures of Researched Molecule P_2 and Control Molecule P_1
See also Scheme S1 and Figures S1–S6.

solution. The introduction of TPE suppressed the intermolecular interactions and limited the intramolecular free rotation of phenyl rings (Zhao et al., 2011, 2012), which solved the problem of aggregation quenching and provided much higher ECL efficiency than that of $Ru(bpy)_3^{2+}$. More crucially, the novel PNs could stably generate high-strength ECL signals at both positive and negative potentials with proper co-reactants. And the mechanism of luminescence was explained by transient ECL test. The new idea of improving ECL efficiency by linking organic molecules with special unit (TPE) has been proposed for the first time, and its universality could be used to improve the ECL efficiency of organic nanoparticles.

RESULTS AND DISCUSSION

Synthesis

Scheme 1 showed the structure of polyfluorene derivative containing TPE (P_2) and its control molecule, P_1. The synthesis routes were detailed in Scheme S1, and the NMR characterization of all molecules and corresponding monomers were given in Figures S1–S6. Briefly, the compounds were synthesized through Suzuki coupling polymerization using Pd as the catalyst. The yields for P_1 and P_2 were 75% and 60%, respectively. The terminal carboxyl groups provide sites for the future bio-orthogonal binding. Furthermore, the corresponding organic nanoparticles PNs-1 and PNs-2 were prepared in aqueous solution using the reprecipitation method (Feng et al., 2016; Suk et al., 2011a, 2011b).

Spectroscopic Characterization of Polymers and PNs

The optical properties of P_1, P_2, and the corresponding organic nanoparticles were systematically characterized and shown in Figures 1A and 1B. For UV–vis absorption spectra, the absorption peaks at 376 and 362 nm belonging to P_1 and P_2, respectively, which could be attributed to $\pi-\pi^*$ transition of the entire conjugated skeleton. The PL spectra of P_1 showed the emission maxima at 414 nm, whereas the PL spectra of P_2 showed the emission peak at 429 nm and a shoulder at 455 nm. For the optical properties of PNs-1 and PNs-2, it was noteworthy that the Stokes shift increasing from 4,314.3 cm^{-1} (P_2) to 7,090.4 cm^{-1} (PNs-2), but it barely showed obvious change between those of P_1 and PNs-1. The larger Stokes shift could be ascribed to the conformational change (Omer et al., 2011). In addition, the PL lifetime of PNs-2 was longer than that of P_2 (Figure S7). Details of all the optical properties were shown in Table 1.

AIE Effect

The difference of fluorescence performance exhibited by P_1 and P_2 in aggregate state was examined. The PL spectra of P_1 and P_2 in tetrahydrofuran (THF)/water mixtures with different water fractions were shown in Figure S8. With increase water fraction, the PL intensity of P_2 increased remarkably (Figure 1C). I_0 and I are the PL intensities of P_2 dissolved in pure THF and THF/water mixtures, respectively. It was worth noting that when the water faction was 90%, the PL intensity of P_2 was 23.2 times that of pure organic phase, indicating an AIE property (Hong et al., 2009; Hu et al., 2014; Liang et al., 2015). On the contrary, P_1 showed aggregation caused quenching (ACQ) effect (Figure S9). The absolute fluorescence quantum efficiencies (QY_{PL}) also proved the ACQ and AIE properties of P_1 and P_2 (Figure S10 and Table 1). It means that in aggregate state, π-π stacking interactions of polyfluorene molecule normally cause ACQ. However, TPE unit could prevent this from happening. In addition, intramolecular rotation is restricted in aggregate state, which blocks the nonradiative pathway and enhances the radiative decay (Zhao et al., 2011, 2012). Figures S11A and 1D showed the HRTEM images of PNs-1 and PNs-2. The morphologies of both PNs are similar with the average diameter of about 9 nm. The dynamic light scattering (DLS) in Figure S12 revealed the

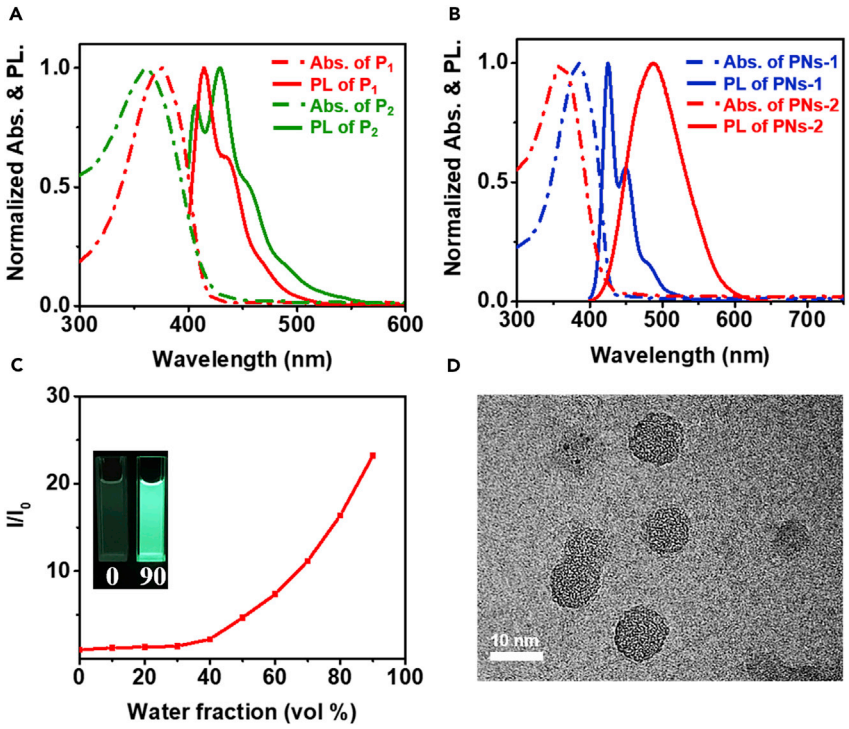

Figure 1. The Spectroscopic and Orphological Characterizations of the Polymers and PNs

(A) Absorbance (dashed curve) and PL spectra (solid curve) of P_1 (red) and P_2 (green) in a solution of MeCN:benzene = 1:1. λ_{exc} = 350 nm.

(B) Absorbance (dashed curve) and PL spectra (solid curve) of PNs-1 (blue) and PNs-2 (red) in aqueous solution. λ_{exc} = 350 nm.

(C) AIE effect of P_2. Plots of I/I_0 vs water fractions in THF/water mixtures (10 μM), where I_0 and I are the PL intensities in pure THF and THF/water mixtures, respectively. Inset: Photographs of P_2 in THF/water mixtures (0, 90%) taken under 365 nm UV lamp.

(D) High-resolution TEM image of 9 nm PNs-2. Scale bar, 10 nm. Data are represented as mean ± TEM.

See also Figures S7–S12.

similar hydrodynamic diameter of PNs-1 (10.13 nm) and PNs-2 (10.82 nm). And PNs-2 is negatively charged with the zeta potential of −33.1 mV, which is attributed to the carboxyl functional group.

Electrochemistry

The electrochemical and ECL performances of P_1, P_2, and corresponding organic nanoparticles were investigated. Figure 2A displayed the cyclic voltammograms (CVs) of P_1 and P_2 in acetonitrile and benzene-mixed solution containing 0.1 M $TBAPF_6$ as the supporting electrolyte. At the scan rate of 0.1 V/s, both P_1 and P_2 showed a pair of well-defined quasi-reversible redox waves, with the similar formal potentials at +1.25 V and +1.27 V vs. SCE, respectively, which could be ascribed to the P/P^+ redox reactions. Upon scanning toward the negative direction, CVs showed irreversible reduction peaks at −2.36 V (P_1) and −2.38 V (P_2) vs. SCE, which belong to the reduction of fluorene and suggested that the anionic radicals were less stable than the cationic radicals (Prieto et al., 2001).

AIECL Effect

In order to verify the AIECL effect of polyfluorene derivative containing TPE, we measured ECL intensity of P_1 and P_2 dissolved in organic solvent and the corresponding PNs dispersed in aqueous solution, using tri-n-propylamine (TPrA) as the co-reactant. As shown in Figure 2B, ECL intensities of P_1 and P_2 were extremely low, whereas the ECL intensity of P_1 was slightly higher than P_2. We examined the ECL intensities of P_1 and P_2 under the different water fractions. As shown in Figure S13, the ECL intensity of P_2 increased dramatically along with the increased water fraction, which was significantly different from that of P_1. After they were prepared into PNs, the ECL intensity of PNs-2 increased dramatically, which was 24 times that of PNs-1,

	λ_{abs} (nm)	λ_{PL} (nm)[a]	Stoke's Shifts $\Delta\lambda_{st}$ (cm^{-1})	Absolute QY_{PL}[b] (%)	τ_{PL} (ns)
P_1	376	414, 434(sh)	2441.2	81.8	0.92
P_2	362	407, 429, 455(sh)	4314.3	3.5	1.08
PNs-1	384	425, 450(sh), 481	2512.3	21.2	0.81
PNs-2	362	487	7090.4	45	1.84

Table 1. Photophysical Properties of P_1 and P_2 in Organic Solvent and PNs-1 and PNs-2 in Aqueous Solution

[a]λ_{exc} = 350 nm.

[b]Measured by integrated sphere in dichloromethane; sh: shoulder.

as shown in Figure 2C. Moreover, the ECL intensity of PNs-2 was 4,000 times that of P_2 dissolved in organic solvent. The highly efficient ECL was attributed to the limitation of intramolecular rotation and π-π stacking interactions caused by TPE unit (Jiang et al., 2019a, 2019b; Liu et al., 2019a, 2019b). Therefore, the most commonly used $Ru(bpy)_3^{2+}$/TPrA system was selected as the standard for evaluating ECL performance of PNs-2 in aqueous solution. The ECL intensity-time curves for the same concentration of $Ru(bpy)_3^{2+}$ and PNs-2 were shown in Figure 2D. The ECL intensity of PNs-2 was slightly lower but quite stable compared with $Ru(bpy)_3^{2+}$ under the condition of 75 mM TPrA as a co-reactant. The effect of TPrA concentration was also investigated and shown in Figure S14. It is worth noting that when the concentration of TPrA decreased below 50 mM, the ECL intensity of PNs-2 began to exceed $Ru(bpy)_3^{2+}$. And the spectral response of the PMT should be considered when the relative ECL efficiency of PNs-2 compared with $Ru(bpy)_3^{2+}$ was calculated. The cathode radiant sensitivity and quantum efficiency vs. wavelength of the PMT applied in this work were shown in Figure S15. At the maximum emission wavelengths of PNs-2 (λ_{max} = 481 nm) and $Ru(bpy)_3^{2+}$ (λ_{max} = 620 nm), the quantum efficiencies of the PMT are very close. Therefore, the ECL intensities of PNs-2 and $Ru(bpy)_3^{2+}$ were not further corrected. This result indicates that PNs-2 dispersed in aqueous solution is definitely a potential high-quality ECL luminophore. Moreover, it also proves that it is quite an effective method to link organic molecules with TPE unit to improve the ECL intensity of organic nanoparticles.

Annihilation ECL

In order to clarify the ECL generation mechanism of PNs-2, the particles were modified on the surface of glassy carbon electrode (GCE) and first performed annihilation ECL experiment without co-reactant (Yang et al., 2019). As shown in Figure 3A, when the applied electrode potential was cyclically scanned between +1.4 V and −2.5 V vs. Ag/AgCl, PNs-2 could produce annihilation ECL signals at both positive and negative potentials of +1.25 V and −2.3 V, respectively. Further, the annihilation ECL signal intensity at −2.3 V was significantly higher than that at +1.25 V. And the transient ECL profile was captured using homemade setup by stepping the potential from −2.5 V to +1.4 V vs. Ag/AgCl with the pulse width of 10 ms. As shown in Figure S16, the ECL signal was not obtained when the potential turned from −2.5 V to +1.4 V but showed on the reversal step. In the classic self-annihilation pathway, the excited state PNs-2* was produced by $PNs\text{-}2^+$ and $PNs\text{-}2^-$ generated at oxidation and reduction potentials, respectively (Richter, 2004; Miao, 2008). Therefore, one conclusion could be drawn that the $PNs\text{-}2^-$ obtained by the reduction step was quite unstable and might decompose slowly (Prieto et al., 2001), which become unavailable to maintain the anodic ECL signal. On the other hand, it could be determined that $PNs\text{-}2^+$ was relatively stable. And it was a reasonable explaination for the much higher ECL intensity at −2.3 V than that at +1.25 V. Figures S11B and 3B revealed the ECL spectra of PNs-1 and PNs-2 obtained by the annihilation routes. The ECL peaks centered at 427 nm (PNs-1) and 481 nm (PNs-2), respectively, which were similar to those of the fluorescence spectra, indicating that the excited state of PNs were caused by bandgap transition (Liu et al., 2013).

Co-reactant ECL

Relative to the annihilation reaction, PNs-2 could produce stronger ECL signals in the presence of co-reactants. The ECL generation mechanisms of PNs-2 with TPrA and $K_2S_2O_8$ as the co-reactants at oxidative and reductive potentials were researched in detail. As shown in Figure 3C, both bare GCE and PNs-2 modified GCE had an irreversible oxidation peak at +0.80 V vs. Ag/AgCl, which was attributed to the oxidation of TPrA to produce $TPrA^{\bullet+}$ and then underwent a rapid deprotonation process to form $TPrA^{\bullet}$ (Miao et al., 2002; Sentic et al., 2014). As the potential scan increased, another new oxidation peak appeared

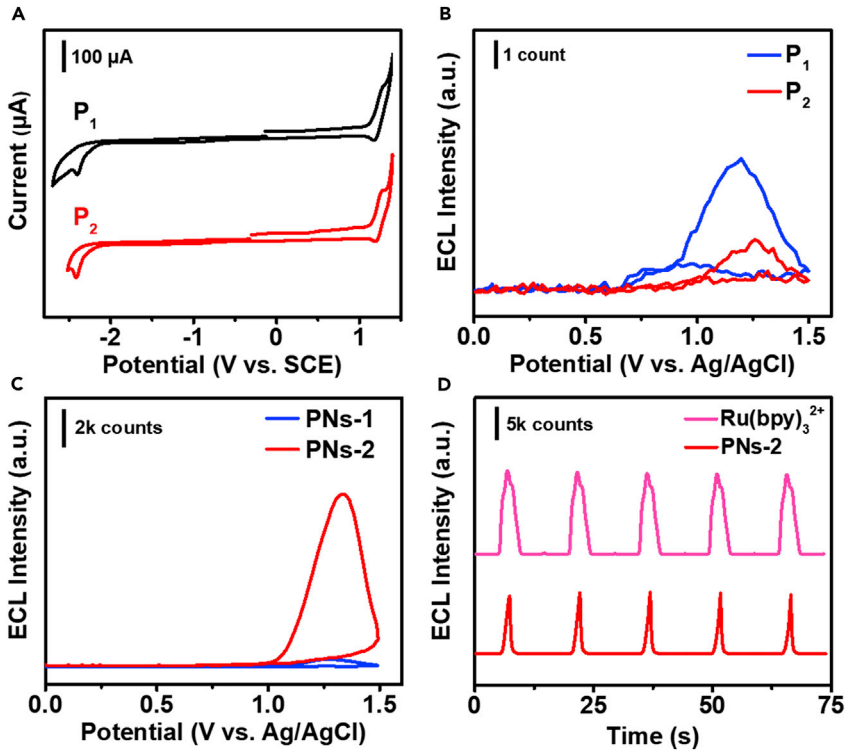

Figure 2. The Electrochemical and ECL Performances of the Polymers and PNs

(A) CVs of 0.5 mM P_1 and P_2 in Bz:MeCN (v:v = 1:1) containing 0.1 M $TBAPF_6$ as the supporting electrolyte with scan rate of 0.1 V/s.

(B) ECL intensity-potential profiles of 20 μM P_1 and P_2 in THF containing 0.1 M $TBAPF_6$ as supporting electrolyte, upon addition of 75 mM TPrA as co-reactant.

(C) ECL intensity-potential profiles of 20 μM PNs-1 and PNs-2 in water containing 0.1 M $LiClO_4$ as the supporting electrolyte, upon addition of 75 mM TPrA as co-reactant.

(D) ECL intensity-time curves of 20 μM PNs-2 and $Ru(bpy)_3^{2+}$ in water containing 0.1 M $LiClO_4$ as the supporting electrolyte with 75 mM TPrA as the co-reactant. PMT = 500 V.

See also Figures S13 and S14.

at +1.29 V, which belonged to the oxidation of PNs-2 to produce PNs-2^+. Meanwhile, strong ECL emission peaked at the same electrode potential. This meant that excited state PNs-2* was generated from the reaction between PNs-2^+ and $TPrA^{\bullet}$. Then the excited state relaxed back to ground state with light radiation. Equations 1, 2, 3, 4, and 5 described the reaction routes using TPrA as the co-reactant.

$$TPrA - e \rightarrow TPrA^{\bullet+} \quad \text{(Equation 1)}$$

$$TPrA^{\bullet+} \rightarrow TPrA^{\bullet} + H^+ \quad \text{(Equation 2)}$$

$$PNs\text{-}2 - e \rightarrow PNs\text{-}2^+ \quad \text{(Equation 3)}$$

$$PNs\text{-}2^+ + TPrA^{\bullet} \rightarrow PNs\text{-}2^* + Pr_2N^+ = CHCH_2CH_3 \quad \text{(Equation 4)}$$

$$PNs\text{-}2^* \rightarrow PNs\text{-}2 + h\nu \quad \text{(Equation 5)}$$

The ECL photograph of PNs-2 modified GCE was taken by camera (inset of Figure 3C). The strong cyan anode ECL emission could even be observed directly with the naked eyes. More importantly, it was easily distinguishable with $Ru(bpy)_3^{2+}$ by wavelength and could be used in combination in cell imaging and

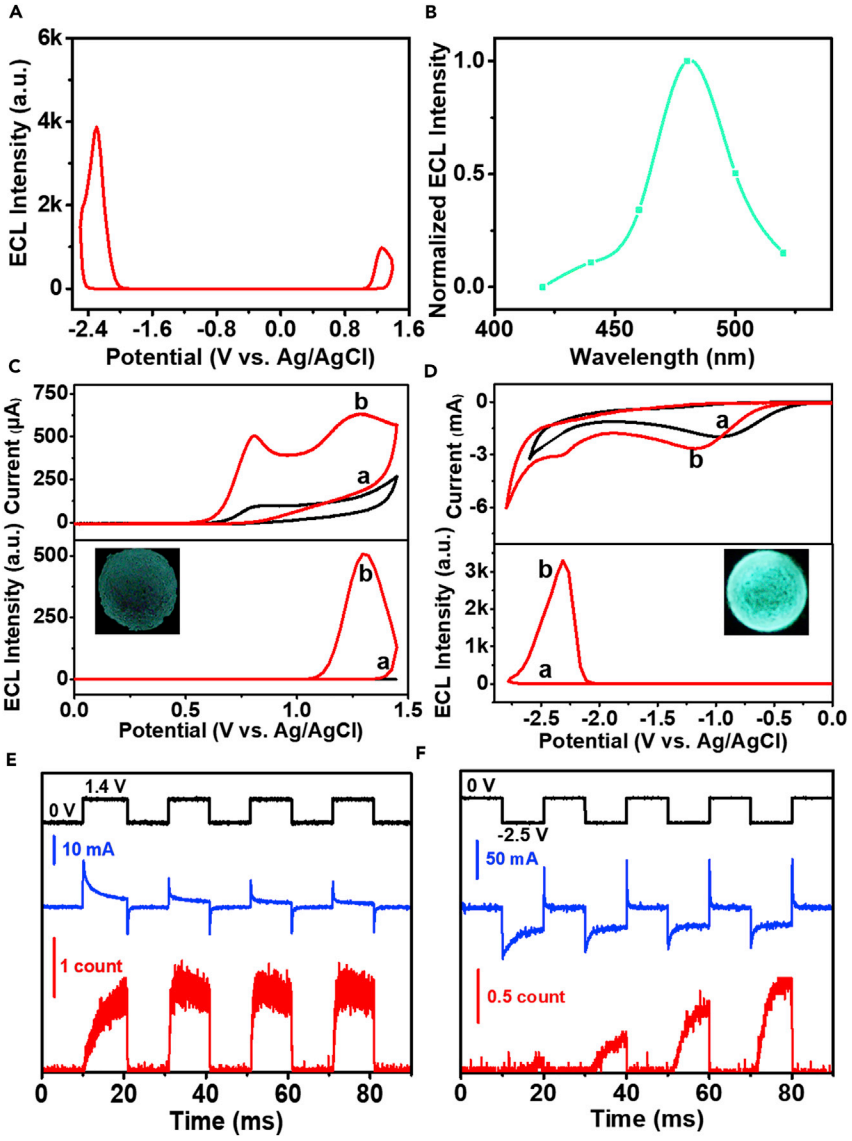

Figure 3. The Annihilation and Co-reactant Route ECL Test of PNs-2

(A) Annihilation ECL intensity-potential curve of PNs-2 modified on GCE surface in water with 0.1 M $LiClO_4$ as supporting electrolyte. Scan rate = 0.10 V s^{-1}. PMT = 500 V.

(B–F) (B) Normalized ECL spectrum of PNs-2 generated through annihilation route by pulsing potential from approximately 100 mV past the peak potentials. CV and ECL intensity-potential profiles of (a) bare GCE and (b) PNs-2 modified GCE in 0.10 M PBS containing (C) 75 mM TPrA and (D) 100 mM $K_2S_2O_8$ as the co-reactant. PMT = 200 V. Inset: ECL photographs of PNs-2 fixed on GCE surface. Transient profiles of current (blue), ECL (red), and applied voltage (black) of PNs-2 modified GCE in 0.10 M PBS containing (E) 75 mM TPrA and (F) 100 mM $K_2S_2O_8$ as co-reactant. The pulse width was 10 ms. PMT = 900 V (E) and 600 V (F).

See also Figures S15–19.

immunoassays (Li et al., 2019). The transient oxidative-process-initiated ECL signal was captured by stepping the potential from 0 V to +1.4 V vs. Ag/AgCl with the pulse width of 10 ms (Figure 3E). The first and last 10 ms data provided a baseline, as the applied voltage was zero and no electrode reaction occurred. Approximately equal ECL signals were observed at each pulse period, indicating that PNs-2 could stably emit over this timescale. The transient ECL signal was obtained immediately when the potential was stepped to +1.4 V, indicating the rapid homogeneous electron transfers rates among the radical ions (Miao et al., 2002). Obviously, as PNs-2 was immobilized on GCE surface, the AIECL effect in solid state greatly

enhanced. And the ECL intensity of PNs-2 was 4.5 times that of $Ru(bpy)_3^{2+}$ modified electrode at the same concentration (Figure S17B). Furthermore, the ECL efficiencies were calculated and compared with those of $Ru(bpy)_3^{2+}$ modified electrode with different concentrations of TPrA (Hesari et al., 2014); the corresponding results were shown in Table S1. It is worth noting that the high relative ECL efficiency of PNs-2 was 163% with 75 mM TPrA. When the concentration of TPrA was reduced to 25 mM, its ECL efficiency was almost three times that of $Ru(bpy)_3^{2+}$. Hence, it could be confirmed that PNs-2 with outstanding ECL efficiency in the positive region has the potential to replace $Ru(bpy)_3^{2+}$ as the best anodic ECL material in aqueous media.

In addition, PNs-2 could also react with $K_2S_2O_8$ to produce a stronger cathodic ECL signal, which deserved our attention. As shown in Figure 3D, the reduction peak of bare GCE at −0.95 V vs. Ag/AgCl was attributed to the reduction of $K_2S_2O_8$ to generate strong oxidant intermediate $SO_4^{-\bullet}$ (Liu et al., 2017). On PNs-2 modified GCE, it was slightly moved to −1.2 V and the reduction current in CV curve became larger. This phenomenon was caused by the reaction between immediately generated strong oxidant intermediate $SO4^{\bullet}$ and PNs-2 to produce positively charged PNs-2^+. Another new reduction peak appeared at −2.3 V belonged to the reduction of PNs-2 to produce PNs-2^-. Meanwhile, the strong cathodic ECL emission peaked at the same potential. There are two possible generation mechanisms of the cathodic ECL. First, $SO_4^{-\bullet}$ may directly react with PNs-2^- to produce the excite state of PNs-2* (Ding et al., 2002; Zhang et al., 2015). Second, $SO_4^{-\bullet}$ could firstly oxidize PNs-2 to produce PNs-2^+, and then the excited state PNs-2* was produced by the annihilation reaction between PNs-2^+ and PNs-2^- (Tan et al., 2017). To figure out the real ECL generation mechanism, transient reductive-process-initiated ECL profile was captured by stepping the potential from 0 V to −2.5 V vs. Ag/Agcl with the pulse width of 10 ms. Similarly, the first and last 10 ms data provided the baseline, as no electrode reaction occurred. As shown in Figure 3F, almost no significant ECL signal was observed when the potential was turned to −2.5 V at the first step. Interestingly, the transient ECL intensity continuously increased during the following steps. As previously mentioned, PNs-2^+ was a quite stable species, but PNs-2^- was clearly not. Considering the fact that the transient ECL signal raised continuously rather than gradually decreased during the cycles, it could be confirmed that the ECL generation mechanism followed the second route. And Equations 6, 7, 8, 9, and 10 described the reaction route between PNs-2 and $K_2S_2O_8$.

$$S_2O_8^{2-} + e \rightarrow SO_4^{2-} + SO_4^{-\bullet} \quad \text{(Equation 6)}$$

$$\text{PNs-2} + SO_4^{-\bullet} \rightarrow \text{PNs-}2^+ + SO_4^{2-} \quad \text{(Equation 7)}$$

$$\text{PNs-2} + e \rightarrow \text{PNs-}2^- \quad \text{(Equation 8)}$$

$$\text{PNs-}2^+ + \text{PNs-}2^- \rightarrow \text{PNs-2*} \quad \text{(Equation 9)}$$

$$\text{PNs-2*} \rightarrow \text{PNs-2} + h\nu \quad \text{(Equation 10)}$$

This is because the cationic radicals generated in each cycle were sufficiently stable to accumulate and resulted in increasing the ECL signal intensity. On the other hand, if the ECL mechanism followed the first route, there would not be continuously enhanced responses. More critically, the reductive initiated ECL signal of PNs-2 was significantly stronger than that of the oxidative progress. It was approximately 6.5 times higher under the optimal experiment conditions (Figure S18). As shown in the inset of Figure 3D, the cathode ECL emission was also bright cyan. As far as we know, this is the first report of water-soluble nanoparticles modified on GCE surface with ultra-high ECL intensity and efficiency at both positive and negative potentials and showed excellent stability (Figure S19).

Conclusion

In summary, we successfully synthesized tetraphenylethylene-containing polyfluorene nanoparticles, which exhibited strong AIECL in aqueous solution. The TPE units limit the stacking interactions of molecules, thus enhancing the ECL signal of nanoparticles. And this TPE copolymerization method perfectly solved the problem of easy quenched and low ECL efficiency of the organic nanoparticles under the aqueous condition. With the suitable co-reactants (TPrA and $S_2O_8^{2-}$), the copolymer nanoparticles showed visualized ECL

emission at both positive and negative potentials. The ECL efficiency is far more than traditional $Ru(bpy)_3^{2+}$ and showed excellent stability. The transient oxidative and reductive initiated ECL profiles were recorded to clarify the mechanism of ECL reactions. This work provides a reference for molecular design of subsequent aqueous-phase ECL emitters and shows promising potential in the development of luminescent device and research of bioanalysis.

Limitations of the Study

Since the AIECL effect depends on the preparation process of the nanoparticles, if the experimental steps given by us are not strictly followed, the nanoparticles with significant enhancement effect will not be obtained.

METHODS

All methods can be found in the accompanying Transparent Methods supplemental file.

SUPPLEMENTAL INFORMATION

Supplemental Information can be found online at https://doi.org/10.1016/j.isci.2019.100774.

ACKNOWLEDGMENTS

This work was supported by the National Natural Science Foundation of China (21535003, 21674046) and the Excellent Research Program of Nanjing University (ZYJH004).

AUTHOR CONTRIBUTIONS

S.J., J.X., and H.C. designed the project; H.G. synthesized the polymers; J.P. and C.X. built the ECL transient instrument; S.J. performed the optical characterization and ECL tests; S.J., Z.W., Y.Q., and J.X. analyzed and discussed the data; S.J. and W.Z. wrote the paper.

DECLARATION OF INTERESTS

The authors declare no competing interests.

Received: September 12, 2019
Revised: November 12, 2019
Accepted: December 9, 2019
Published: January 24, 2020

REFERENCES

Carrara, S., Aliprandi, A., and De Cola, L. (2017). Aggregation-induced electrochemiluminescence of platinum (II) complexes. J. Am. Chem. Soc. *139*, 14605–14610.

Carrara, S., Stringer, B., and Hogan, C.F. (2018). Unusually strong electrochemiluminescence from iridium-based redox polymers immobilized as thin layers or polymer nanoparticles. ACS Appl. Mater. Interfaces *10*, 37251–37257.

Chang, Y.L., Bard, A.J., and Barbara, P.F. (2008). Electrogenerated chemiluminescence of single conjugated polymer nanoparticles. J. Am. Chem. Soc. *130*, 8906–8907.

Deng, S.Y., and Ju, H.X. (2013). Electrogenerated chemiluminescence of nanomaterials for bioanalysis. Analyst *138*, 43–61.

Ding, Z.F., Korgel, B.A., and Bard, A.J. (2002). Electrochemistry and electrogenerated chemiluminescence from silicon nanocrystal quantum dots. Science *296*, 1293–1297.

Feng, Y.Q., Ju, H.X., and Cheng, Y.X. (2016). Silole-containing polymer nanodot: an aqueous low-potential electrochemiluminescence emitter for biosensing. Anal. Chem. *88*, 845–850.

Gao, T.B., Jiang, D.C., and Ye, D.J. (2018). Aggregation-induced electrochemiluminescence from a cyclometalated iridium (III) complex. Inorg. Chem. *57*, 4310–4316.

Guo, W.L., Su, B., and Shao, Y.H. (2018). Potential-resolved multicolor electrochemiluminescence for multiplex immunoassay in a single sample. J. Am. Chem. Soc. *140*, 15904–15915.

Han, Z.G., Yang, Z.F., and Lu, X.Q. (2019). Electrochemiluminescence platforms based on small water-insoluble organic molecules for ultrasensitive aqueous-phase detection. Angew. Chem. Int. Ed. *131*, 5976–5980.

Hesari, M., Workentin, M.S., and Ding, Z.F. (2014). Highly efficient electrogenerated chemiluminescence of Au_{38} nanoclusters. ACS Nano *8*, 8543–8553.

Hong, Y.N., Lam, J.W.Y., and Tang, B.Z. (2009). Aggregation-induced emission: phenomenon, mechanism and applications. Chem. Commun. (Camb.) *29*, 4332–4353.

Honmou, Y., Iyoda, T., and Vacha, M. (2014). Single-molecule electroluminescence and photoluminescence of polyfluorene unveils the photophysics behind the green emission band. Nat. Commun. *5*, 4666.

Hu, R.R., Leung, N.L.C., and Tang, B.Z. (2014). AIE macromolecules: syntheses, structures and functionalities. Chem. Soc. Rev. *43*, 4494–4562.

Jiang, H., Liu, L., and Wang, X.M. (2019a). Aggregation-induced electrochemiluminescence by metal-binding protein responsive hydrogel scaffolds. Small *15*, 1901170.

Jiang, M.H., Zhuo, Y., and Yuan, R. (2019b). Electrochemiluminescence enhanced by restriction of intramolecular motions (RIM): tetraphenylethylene microcrystals as a novel

emitter for mucin 1 detection. Anal. Chem. *91*, 3710–3716.

Josh, V.W., Ratner, M.A., and Wasielewski, M.R. (2010). Crossover from single-step tunneling to multistep hopping for molecular triplet energy transfer. Science *328*, 1547–1550.

Knaapila, M., and Monkman, A.P. (2013). Methods for controlling structure and photophysical properties in polyfluorene solutions and gels. Adv. Mater. *25*, 1090–1108.

Li, C.P., Wang, S.S., and Jin, Y.D. (2019). Nanoengineered metasurface immunosensor with over 1000-Fold electrochemiluminescence enhancement for ultra-sensitive bioassay. iScience *17*, 267–276.

Liang, J., Tang, B.Z., and Liu, B. (2015). Specific light-up bioprobes based on AIEgen conjugates. Chem. Soc. Rev. *44*, 2798–2811.

Liu, S.F., Zhang, X., and Zou, G.Z. (2013). Bandgap engineered and high monochromatic electrochem-iluminescence from dual-stabilizers-capped CdSe nanocrystals with practical application potential. Biosens. Bioelectron. *55*, 203–208.

Liu, H.W., Qi, H.L., and Gao, Q. (2017). Aggregation-induced enhanced electrochemiluminescence from organic nanoparticles of donor-acceptor based coumarin derivatives. ACS Appl. Mater. Interfaces *9*, 44324–44331.

Liu, J.L., Chai, Y.Q., and Yuan, R. (2019a). Near-infrared aggregation-induced enhanced electrochemiluminescence from tetraphenylethylene nanocrystals: a new generation of ECL emitters. Chem. Sci. *10*, 4497–4501.

Liu, J.L., Chai, Y.Q., and Yuan, R. (2019b). BSA stabilized tetraphenylethylene nanocrystals as aggregation-induced enhanced electrochemiluminescence emitters for ultrasensitive microRNA assay. Chem. Commun. (Camb.) *55*, 9959–9962.

Miao, W.J. (2008). Electrogenerated chemiluminescence and its biorelated applications. Chem. Rev. *108*, 2506–2553.

Miao, W.J., Choi, J.P., and Bard, A.J. (2002). Electrogenerated chemiluminescence 69: the tris(2,2'-bipyridine) ruthenium (II), ($Ru(bpy)_3^{2+}$)/tri-n-propylamine (TPrA) system revisited a new route involving $TPrA^{\bullet+}$ cation radicals. J. Am. Chem. Soc. *124*, 14478–14485.

Omer, K.M., Ku, S.Y., and Bard, A.J. (2011). Electrochemistry and electrogenerated chemiluminescence of a spirobifluorene-based donor (triphenylamine)-acceptor (2,1,3-benzothiadiazole) molecule and its organic nanoparticles. J. Am. Chem. Soc. *133*, 5492–5499.

O'Carroll, D., Iacopino, D., and Redmond, G. (2008). Poly(9,9-dioctylfluorene) nanowires with pronounced β-phase morphology: synthesis, characterization, and optical properties. Adv. Mater. *20*, 42–48.

Prieto, I., Teetsov, J., and Bard, A.J. (2001). A study of excimer emission in solutions of poly(9,9-dioctylfluorene) using electrogenerated chemiluminescence. J. Phys. Chem. A *105*, 520–523.

Qi, H.L., Rathore, R., and Bard, A.J. (2012). Electrochemistry and electrogenerated chemiluminescence of π-stacked poly(fluorenemethylene) oligomers. multiple, interacting electron transfers. J. Am. Chem. Soc. *134*, 16265–16274.

Richter, M.M. (2004). Electrochemiluminescence (ECL). Chem. Rev. *104*, 3003–3036.

Scherf, U., and List, E.J.W. (2002). Semiconducting polyfluorenes towards reliable structure property relationships. Adv. Mater. *14*, 477–487.

Sentic, M., Milutinovic, M., and Sojic, N. (2014). Mapping electrogenerated chemiluminescence reactivity in space: mechanistic insight into model systems used in immunoassays. Chem. Sci. *5*, 2568–2572.

Suk, J., Cheng, J.Z., and Bard, A.J. (2011a). Synthesis, electrochemistry, and electrogenerated chemiluminescence of Azide-BTA, a D–A−π–A–D species with benzothiadiazole and N,N-Diphenylaniline, and its nanoparticles. J. Phys. Chem. C *115*, 14960–14968.

Suk, J., Wang, L., and Bard, A.J. (2011b). Electrochemistry, electrogenerated chemiluminescence, and excimer formation dynamics of intramolecular π-stacked 9-naphthylanthracene derivatives and organic nanoparticles. J. Am. Chem. Soc. *133*, 14675–14685.

Tan, X., Zhang, B., and Zou, G. (2017). Electrochemistry and electrochemiluminescence of organometal halide perovskite nanocrystals in aqueous medium. J. Am. Chem. Soc. *139*, 8772–8776.

Valenti, G., Scarabino, S., and Sojic, N. (2017). Single cell electrochemiluminescence imaging: from the proof-of-concept to disposable device-based analysis. J. Am. Chem. Soc. *139*, 16830–16837.

Voci, S., Goudeau, B., and Sojic, N. (2018). Surface-confined electrochemiluminescence microscopy of cell membranes. J. Am. Chem. Soc. *140*, 14753–14760.

Voityuk, A.A. (2010). Triplet excitation energy transfer through fluorene π stack. J. Phys. Chem. C *114*, 20236–20239.

Wei, X., Yan, H., and Xu, J.J. (2019a). Aggregation-induced electrochemiluminescence of carboranyl carbazoles in aqueous media. Angew. Chem. Int. Ed. *58*, 3162–3166.

Wei, X., Yan, H., and Xu, J.J. (2019b). Recent advances in aggregation-induced electrochemiluminescence. Chem. Eur. J. *25*, 1–14.

Wong, K.T., Chien, Y.Y., and Wu, C.C. (2002). Ter(9,9-diarylfluorene)s: highly efficient blue emitter with promising electrochemical and thermal stability. J. Am. Chem. Soc. *124*, 11576–11577.

Yang, L.Q., Zhang, B., and Zou, G.Z. (2019). Efficient and monochromatic electrochemiluminescence of aqueous soluble Au nanoclusters via host–guest recognition. Angew. Chem. Int. Ed. *131*, 6975–6979.

Zhang, Y.Y., Feng, Q.M., and Xu, J.J. (2015). Silver nanoclusters for high-efficiency quenching of CdS nanocrystal electrochemiluminescence and sensitive detection of microRNA. ACS Appl. Mater. Interfaces *7*, 26307–26314.

Zhang, J.J., Jiang, D.C., and Chen, H.Y. (2019). Electrochemiluminescence-based capacitance microscopy for label-free imaging of antigens on the cellular plasma membrane. J. Am. Chem. Soc. *141*, 10294–10299.

Zhao, Z.J., Chen, S.M., and Tang, B.Z. (2011). Construction of efficient solid emitters with conventional and AIE luminogens for blue organic light-emitting diodes. J. Mater. Chem. *21*, 10949–10956.

Zhao, Z.J., Chan, C.Y.K., and Tang, B.Z. (2012). Using tetraphenylethene and carbazole to create efficient luminophores with aggregation-induced emission, high thermal stability, and good hole-transporting property. J. Mater. Chem. *22*, 4527–4534.

ISCI, Volume *23*

Supplemental Information

Highly Efficient Aggregation-Induced Electrochemiluminescence of Polyfluorene Derivative Nanoparticles Containing Tetraphenylethylene

Si-Yuan Ji, Wei Zhao, Hang Gao, Jian-Bin Pan, Cong-Hui Xu, Yi-Wu Quan, Jing-Juan Xu, and Hong-Yuan Chen

SUPPLEMENTAL FIGURES

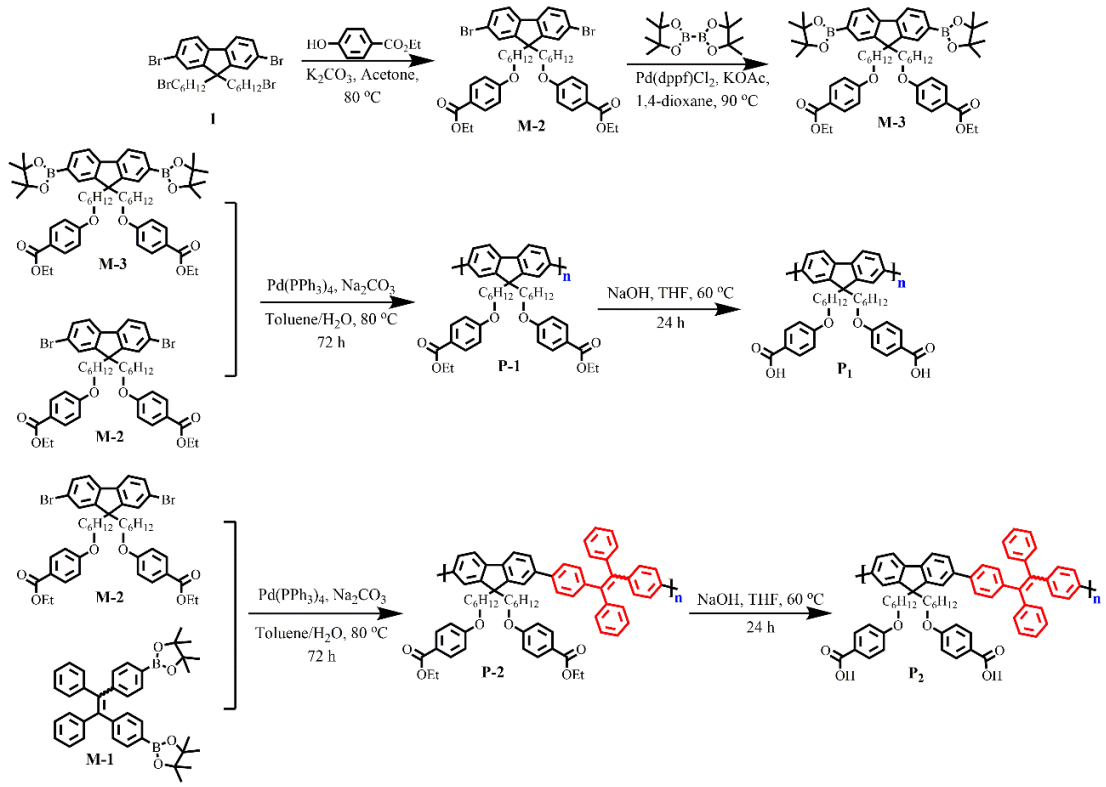

Scheme S1. The synthesis route of the polymers (P_1 and P_2). Related to Scheme 1.

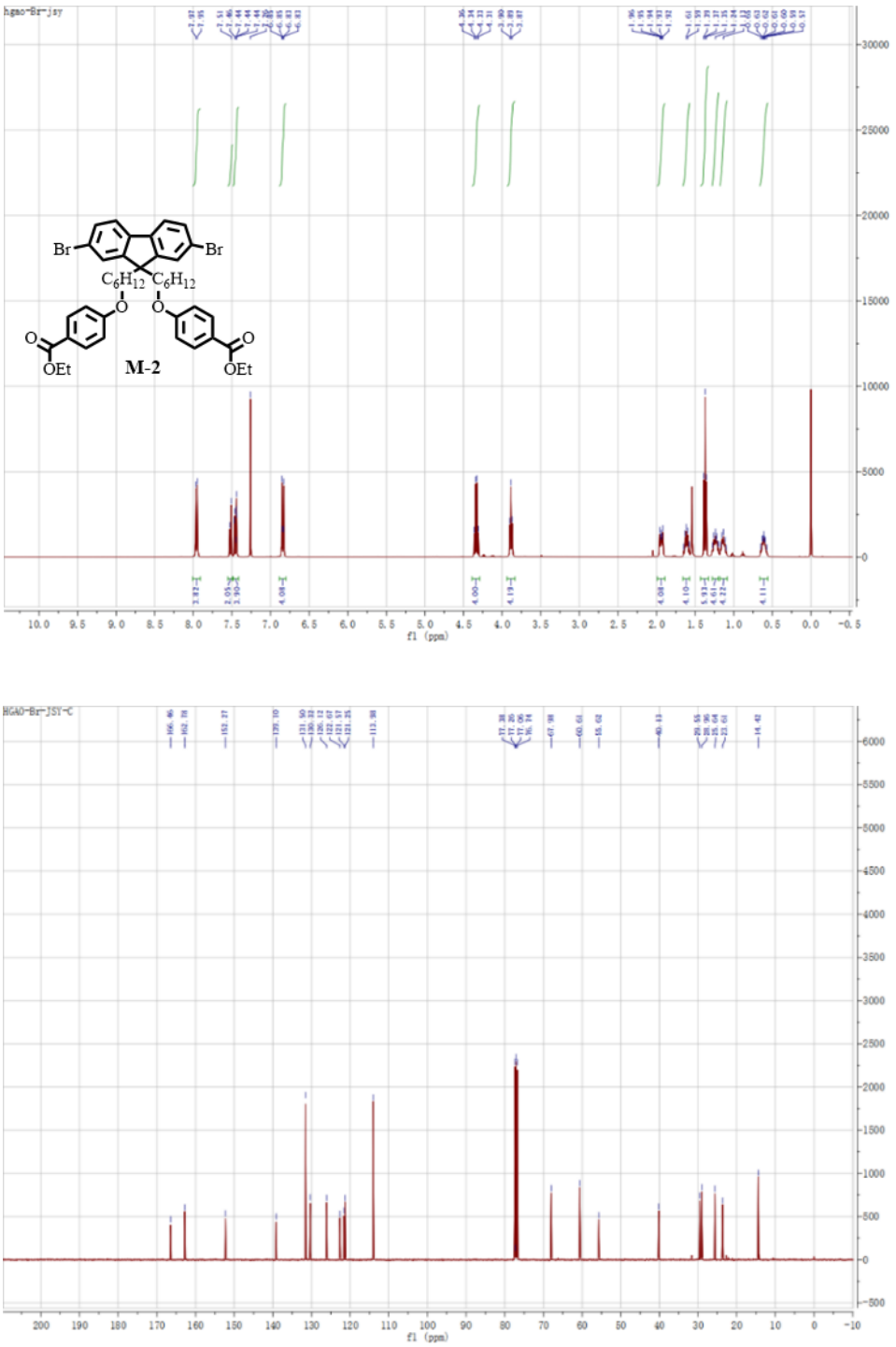

Figure S1. ^{1}H (400 MHz, $CDCl_3$, 25°C) and ^{13}C (100 MHz, $CDCl_3$, 25°C) NMR Spectra of **M-2.** Related to Scheme 1.

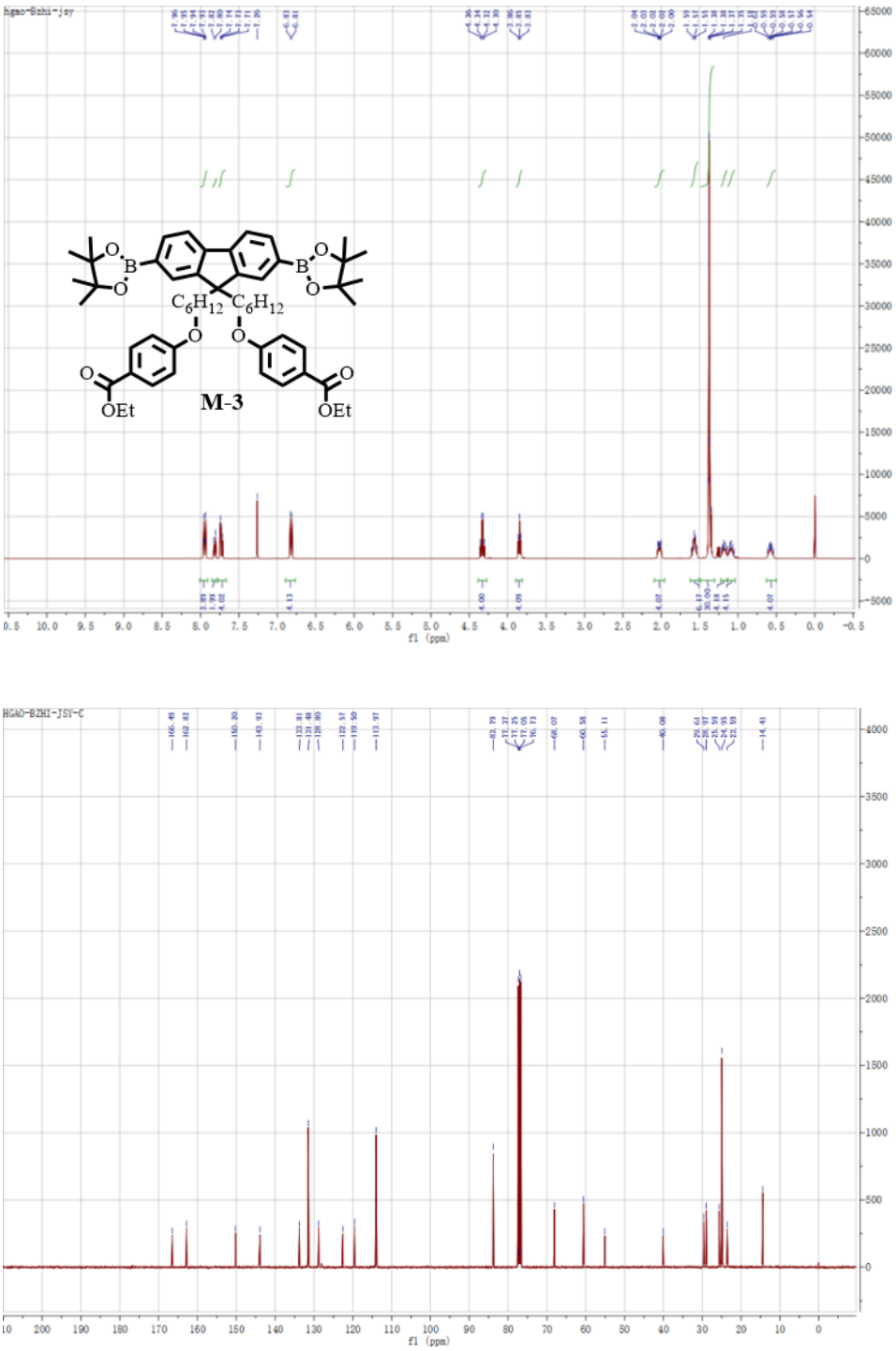

Figure S2. ^{1}H (400 MHz, $CDCl_3$, 25°C) and ^{13}C (100 MHz, $CDCl_3$, 25°C) NMR Spectra of **M-3.** Related to Scheme 1.

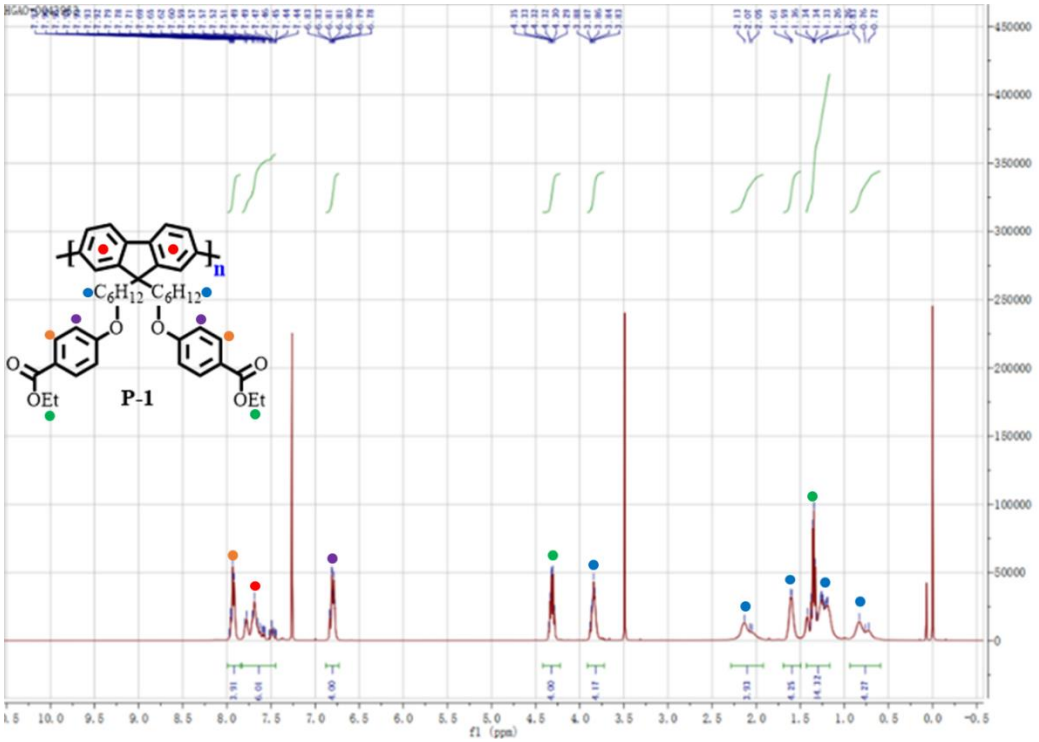

Figure S3. ^{1}H (400 MHz, $CDCl_3$, 25ºC) NMR Spectra of **P-1.** Related to Scheme 1.

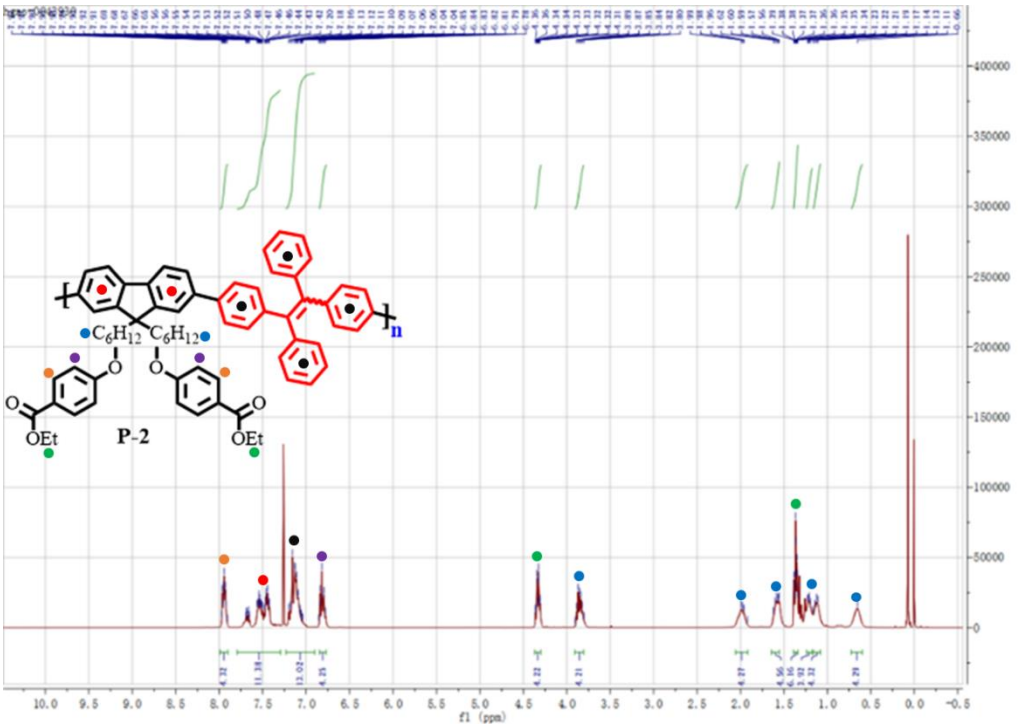

Figure S4. ^{1}H (400 MHz, $CDCl_3$, 25ºC) NMR Spectra of **P-2.** Related to Scheme 1.

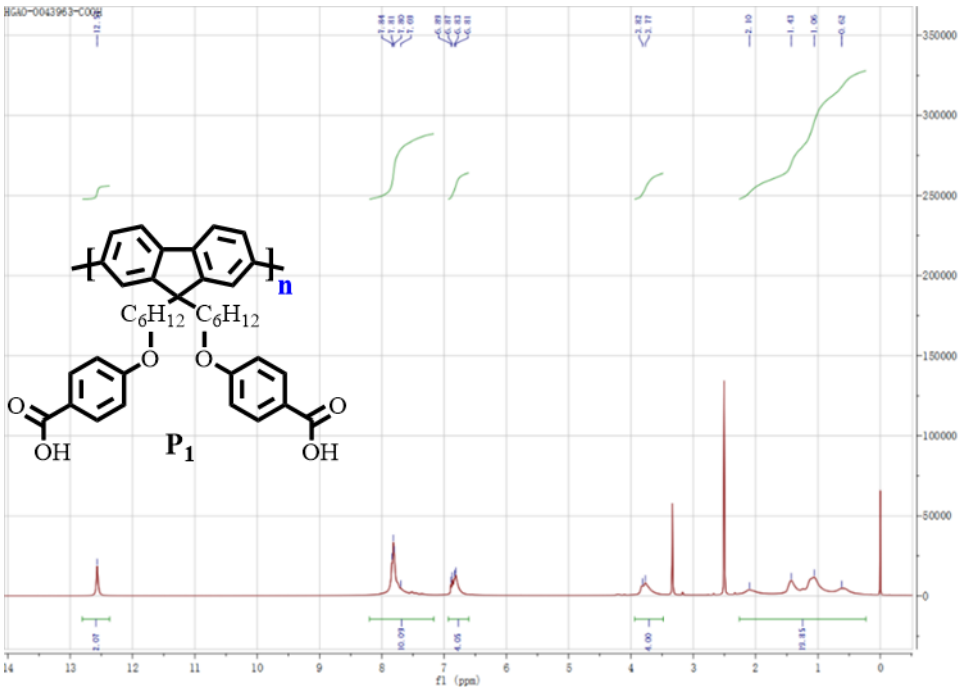

Figure S5. ^{1}H (400 MHz, DMSO-d6, 25°C) NMR Spectra of **P_1.** Related to Scheme 1.

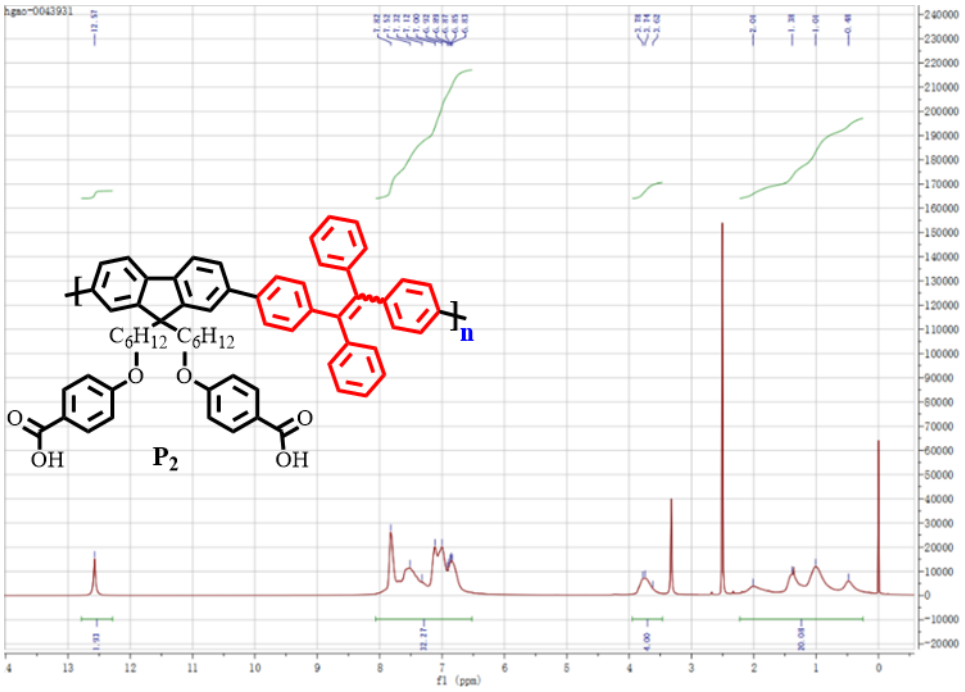

Figure S6. ^{1}H (400 MHz, DMSO-d6, 25°C) NMR Spectra of **P_2.** Related to Scheme 1.

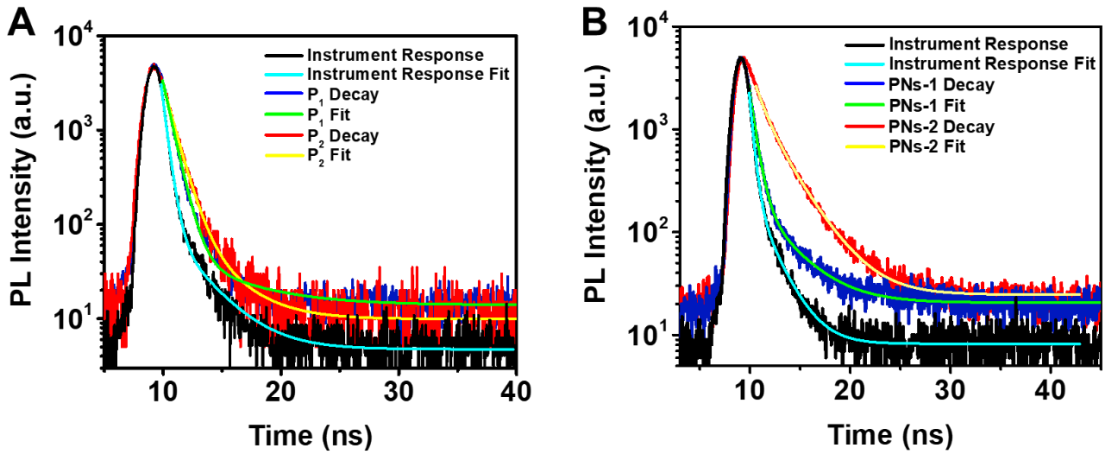

Figure S7. The PL lifetime decay curves of (A) P_1 and P_2, (B) PNs-1 and PNs-2. The pulse width of the pulsed excitation source is 998.5 ps. Related to Figure 1 and Table 1.

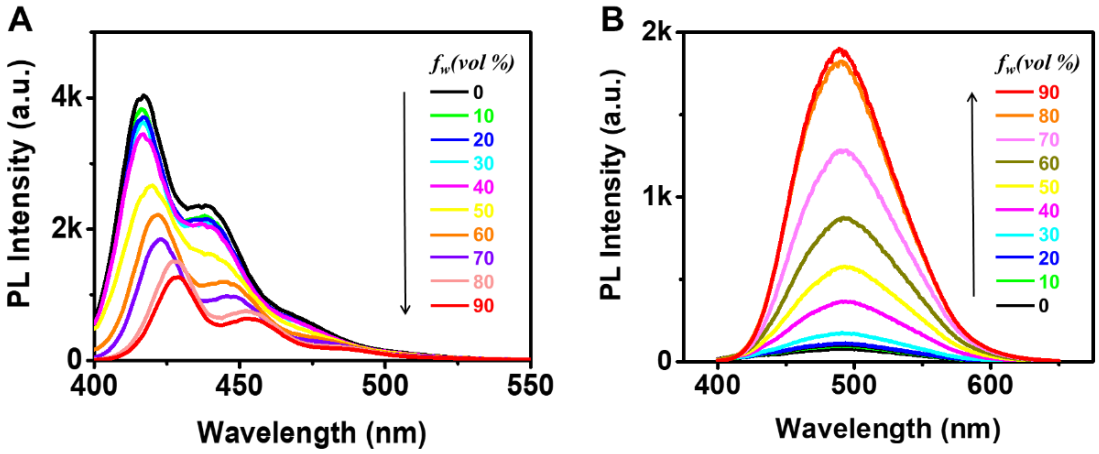

Figure S8. The PL spectra of (A) P_1 and (B) P_2 in THF/water mixtures with different water fractions (f_w). Related to Figure 1.

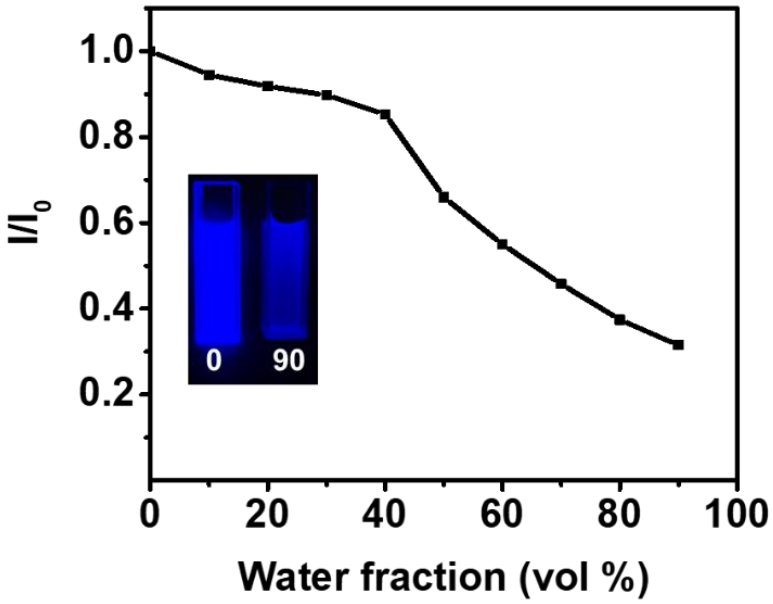

Figure S9. ACQ effect of P_1. Plots of I/I_0 vs water fractions in THF/water mixtures (10 μM), where I_0 and I were the PL intensities in pure THF and THF/water mixtures, respectively. Inset: Photographs of P_1 in THF/water mixtures (0, 90%) taken under 365 nm UV lamp. Related to Figure 1.

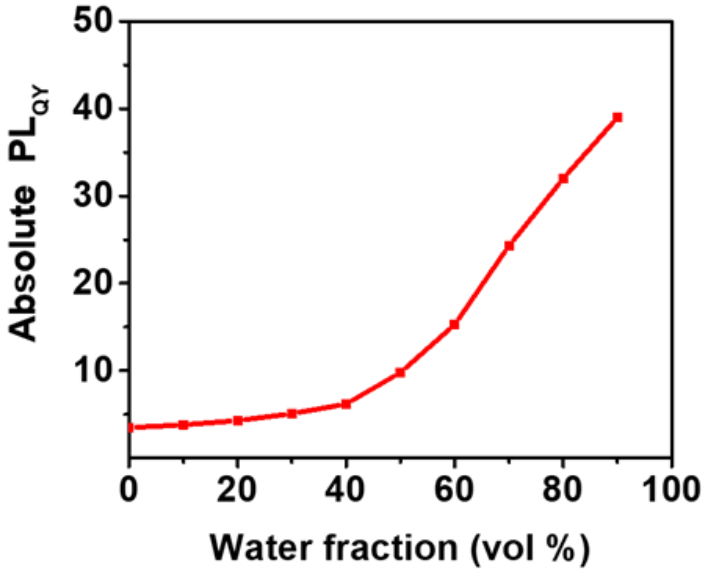

Figure S10. Plot of absolute fluorescence quantum efficiencies (QY_{PL}) of P_2 vs water fractions in THF/H_2O mixtures (10 μM). Related to Figure 1

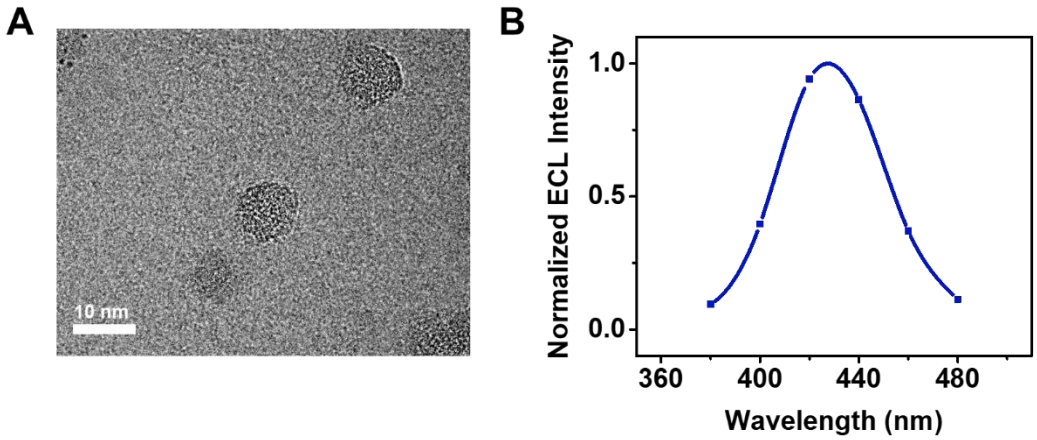

Figure S11. (A) High-resolution TEM image of 9 nm PNs-1. Scale bar, 10 nm. Data are represented as mean ± TEM. (B) Normalized ECL spectrum of PNs-1 generated through annihilation route by pulsing potential from approximately 100 mV past the peak potentials. Related to Figure 1 and Figure 3.

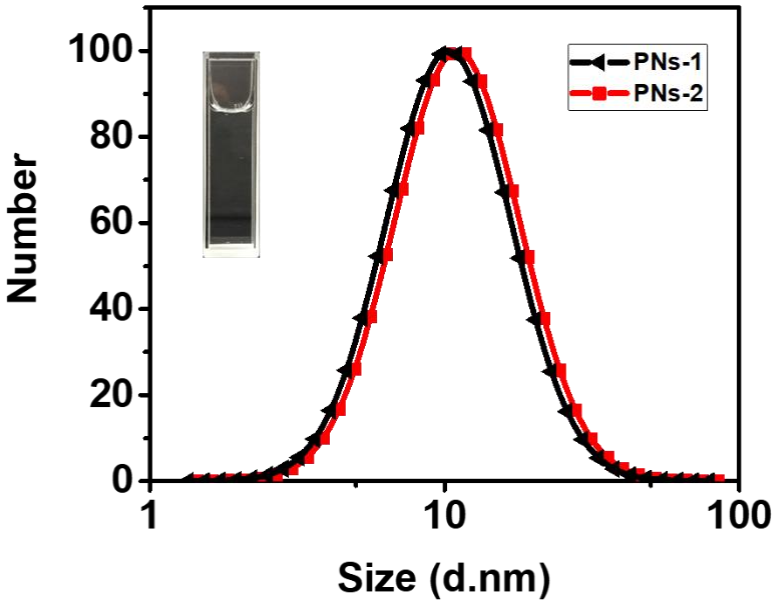

Figure S12. The DLS size distribution of the PNs-1 and PNs-2. Inset: Photograph of PNs-2 aqueous solution. Related to Figure 1.

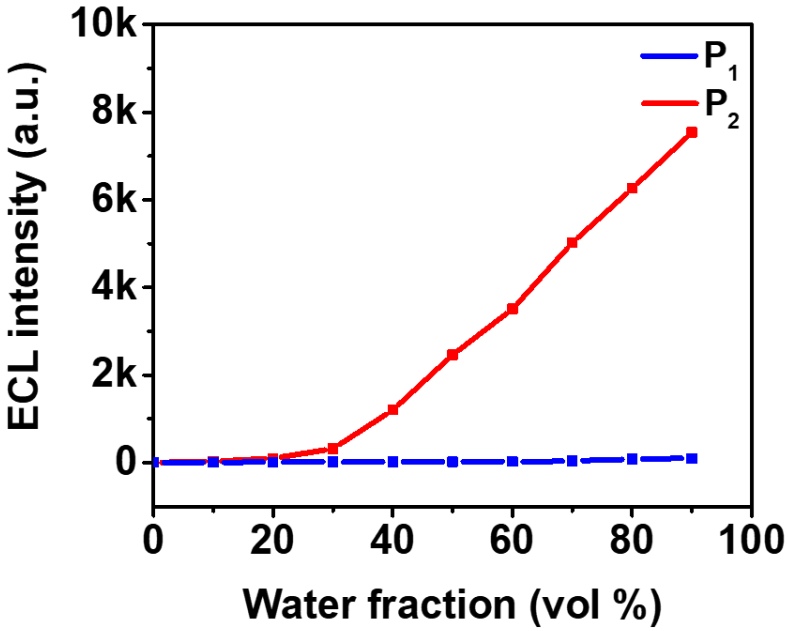

Figure S13. Plot of the ECL intensity changes of P_1 (blue) and P_2 (red) upon variation of the H_2O fraction of the THF/H_2O mixtures, upon addition of 75 mM TPrA as co-reactant. PMT = 500 V. Related to Figure 2.

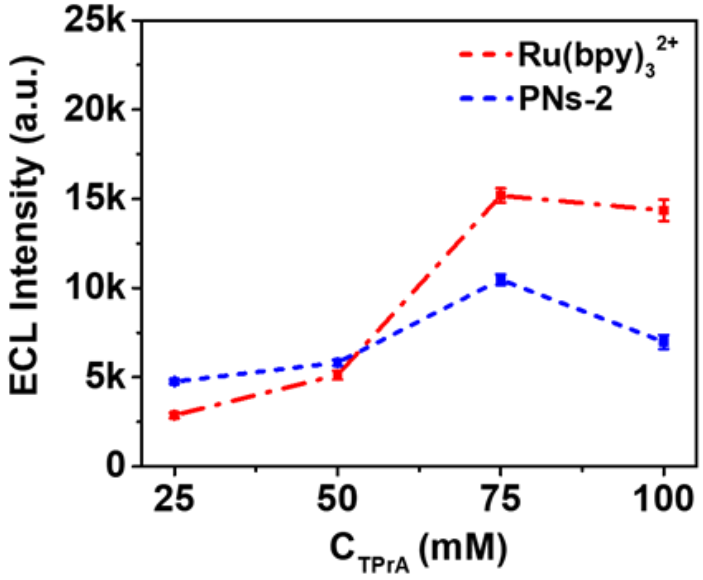

Figure S14. Effect of TPrA concentration on the ECL intensity of 20 μM PNs-2 (blue) or $Ru(bpy)_3^{2+}$ (red) in water containing 0.1 M $LiClO_4$ as the supporting electrolyte. PMT = 500 V. Related to Figure 2.

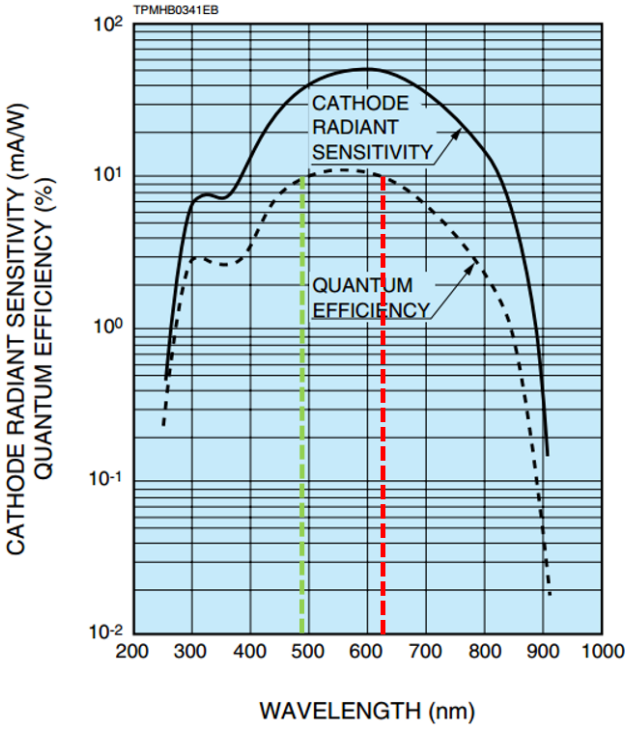

Figure S15. The spectral response curve of Hamamatsu R2257 PMT used in our ECL test. Related to Figure 2 and 3.

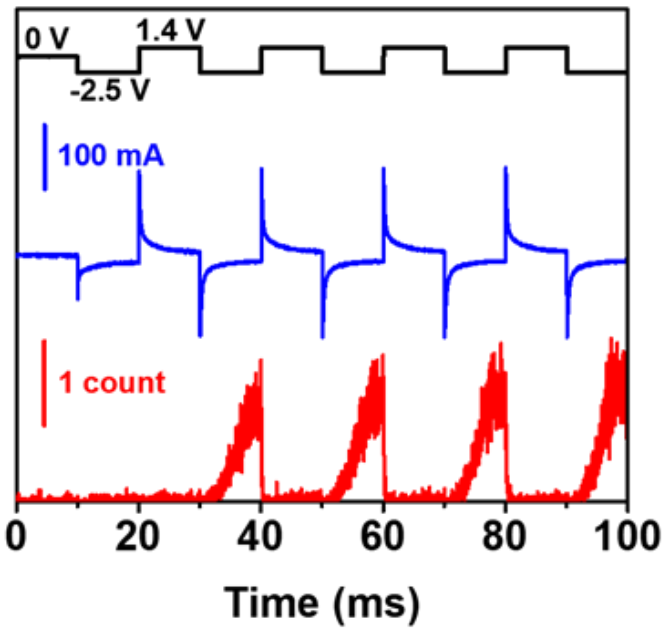

Figure S16. Transient profiles of current (blue), ECL (red) and applied voltage (black) of PNs-2 modified GCE in 0.10 M PBS. The applied potential was repetitively stepped from -2.5 V to +1.4 V vs Ag/AgCl and the pulse width is 10 ms. Related to Figure 3.

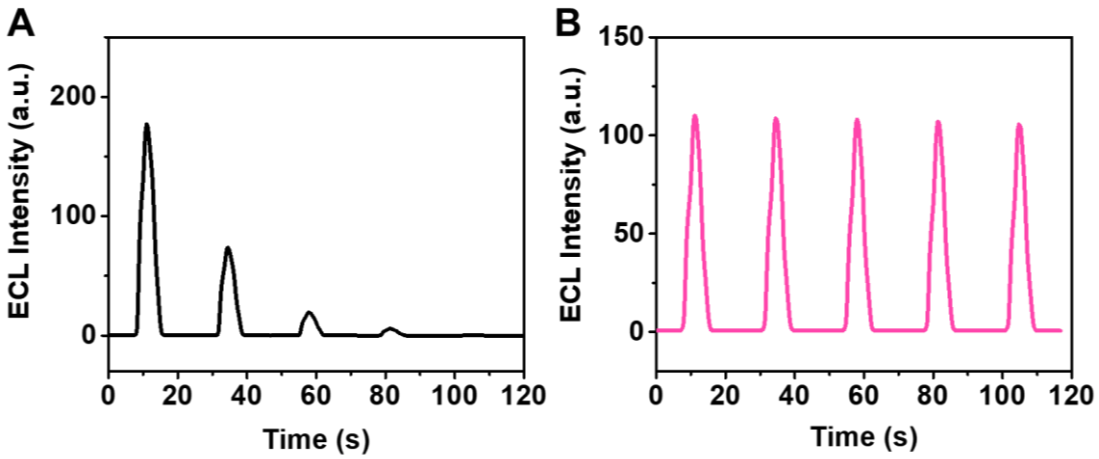

Figure S17. ECL intensity−time curves of 20 μM $Ru(bpy)_3^{2+}$ modified GCE (A) without Nafion and (B) with Nafion in 0.1 M PBS solution containing 75 mM TPrA as co-reactant. PMT = 200 V. Related to Figure 3.

Table S1. Calculated ECL Efficiency for PNs-2 Relative to That of 20 μM $Ru(bpy)_3^{2+}$ (Nafion) Under Different Concentrations of TPrA.

C_{TPrA} (mM)	Relative ECL Efficiency (%)
25	286
50	242
75	163
100	145

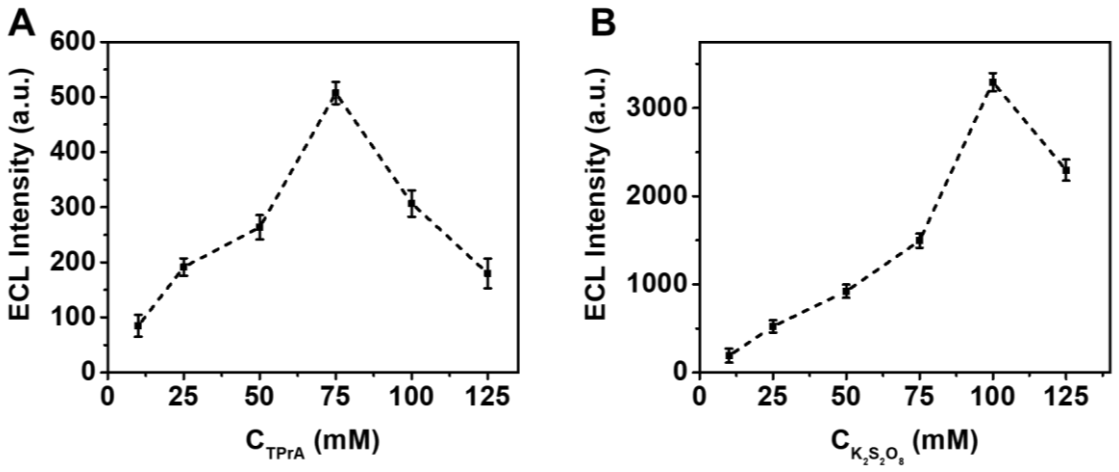

Figure S18. The optimization of experiment conditions. Effects of (A) TPrA and (B) $K_2S_2O_8$ concentration on the ECL intensity of the PNs-2 modified GCE. PMT = 200 V. Related to Figure 3.

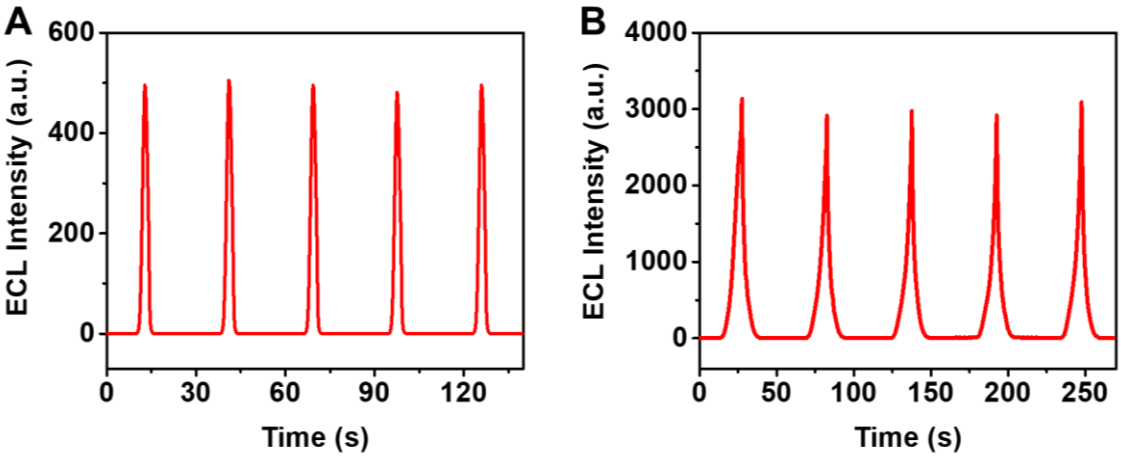

Figure S19. ECL intensity−time curves of PNs-2 modified GCE in 0.1 M PBS solution containing (A) 75 mM TPrA and (B) 100mM $K_2S_2O_8$ as co-reactant. PMT = 200 V. Related to Figure 3.

Transparent Methods

Reagents and materials.

All the chemicals were used as received without further purification. Anhydrous benzene (Bz, 99.8%), tetra-n-butylammonium hexafluorophosphate ($TBAPF_6$), tetrahydrofuran (THF, 99.9%), electrochemical-grade anhydrousacetonitrile (MeCN, 99.8%), Nafion® perfluorinated resin solution (5.0 wt%), lithium perchlorate ($LiClO_4$) and tris(2,2'-bipyridyl) dichlororuthenium (II) hexahydrate ($Ru(bpy)_3^{2+}$) were purchased from Sigma-Aldrich (USA) and stored into a dry-box. Tripropylamine (TPrA, 98%) and $K_2S_2O_8$ were purchased from Aladdin Reagent Corporation (Shanghai, China). Phosphate buffer saline (PBS, 0.1 M, pH 7.4) was prepared by mixing stock solution of NaH_2PO_4 and Na_2HPO_4 that contained 0.1 M NaCl. Ultrapure fresh water was obtained from the Millipore water purification system (resistivity of 18.2 MΩ·cm at 25 °C) and used for preparation of all aqueous solutions.

M-2

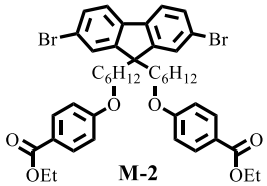

M-2

Compound **1** (2.75 g, 4.23 mmol), 4-hydroxybenzoic acid ethyl ester (2.11 g, 12.7 mmol) and K_2CO_3 (2.9 g, 21.15 mmol) were dissolved in 50 mL of acetone, and the reaction mixture was heated at 80 °C for overnight. After the reaction mixture was cooled to room temperature, the solution was filtered. The solvent was removed under reduced pressure, and the residue was purified by silica gel column chromatography (eluent: petroleum ether/ethyl acetate, v/v, 15:1) to give **M-2** as white solid (2.9 g, 84%). ^{1}H NMR (400 MHz, $CDCl_3$) δ (ppm): 7.97–7.95 (m, 4H), 7.53–7.51 (m, 2H), 7.47–7.44 (m, 4H), 6.85–6.83 (m, 4H), 4.34 (q, *J* = 7.1 Hz, 4H), 3.89 (t, *J* = 6.5 Hz, 4H), 1.96–1.92 (m, 4H), 1.65–1.58 (m, 4H), 1.37 (t, *J* = 7.1 Hz, 6H), 1.27–1.20 (m, 4H), 1.178–1.10 (m, 4H), 0.65–0.57 (m, 4H); ^{13}C NMR (100 MHz, $CDCl_3$) δ (ppm): 166.46, 162.78, 152.27, 139.10, 131.50, 130.32, 126.12, 122.67, 121.57, 121.25, 113.98, 67.98, 60.61, 55.62, 40.13, 29.55, 28.96, 25.64, 23.61, 14.42.

M-3

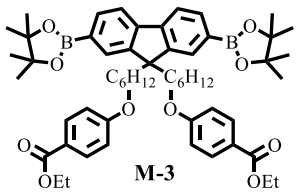

M-3

M-2 (2.5 g, 4.56 mmol), bis(pinacolato)diboron (1.5 g, 5.93 mmol), $Pd(dppf)Cl_2$ (186.2 mg, 0.228 mmol) and KOAc (1.12 g, 11.4 mmol) were added into 20 mL dioxane solvent. The mixture was stirred at 100 °C under N_2 atmosphere. After reaction for 24 h, the solvent was removed under reduced pressure, and residue was purified by silica gel column chromatography (eluent: petroleum ether/ethyl acetate, v/v, 80:1) to afford

M-3 as white solid (2.4 g, 58%). ^{1}H NMR (400 MHz, $CDCl_3$) δ (ppm): 7.96–7.93 (m, 4H), 7.82–7.80 (m, 2H), 7.74–7.71 (m, 4H), 6.83–6.81 (m, 4H), 4.33 (q, *J* = 7.1 Hz, 4H), 3.85 (t, *J* = 6.6 Hz, 4H), 2.04–2.00 (m, 4H), 1.61–1.54 (m, 4H), 1.38–1.35 (m, 30H), 1.22–1.15 (m, 4H), 1.12–1.05 (m, 4H), 0.61–0.54 (m, 4H); ^{13}C NMR (100 MHz, $CDCl_3$) δ (ppm): 166.49, 162.82, 150.20, 143.93, 133.81, 131.48, 128.80, 122.57, 119.50, 113.97, 83.79, 68.07, 60.58, 55.11, 40.08, 29.61, 28.97, 25.59, 24.95, 23.59, 14.41.

P-1

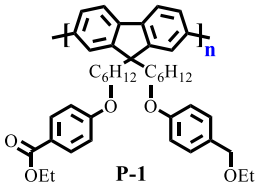

P-1

The mixture of **M-2** (158.8 mg, 0.193 mmol), **M-3** (177.0 mg, 0.193 mmol), $Pd(PPh_3)_4$ (22 mg, 0.0193 mmol), and K_2CO_3 (533 mg, 3.9 mmol) in Toluene/H_2O (8 mL: 2 mL) in a Schlenk tube was stirred at 100 °C for 72 h under the argon atmosphere. After reaction, the resulting polymers were purified by being precipitated in methanol twice. Then the solids were dried in vacuum to afford **P-1** as pale yellow solid (227 mg, 85%). ^{1}H NMR (400 MHz, $CDCl_3$) δ 7.97–7.92 (m, 4H), 7.79–7.44 (m, 6H), 6.83–6.78 (m, 4H), 4.35–4.29 (m, 4H), 3.88–3.83 (m, 4H), 2.13–2.05 (m, 4H), 1.61–1.59 (m, 4H), 1.42–1.19 (m, 14H), 0.83–0.72 (m, 4H).

P_1

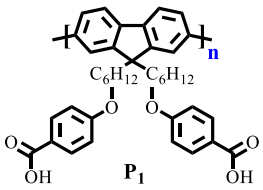

P_1

P-1 (227 mg, 0.329 mmol) and NaOH (262.8 mg, 6.57 mmol) were dissolved in 50 mL THF, and the reaction mixture was heated at 80 °C overnight. After the reaction mixture was cooled to room temperature, the solution was adjusted pH to ~2 followed by filtration. The solvent was removed under reduced pressure, and the residue was purified by being precipitated in methanol twice. Then the solids were dried in vacuum to afford **P_1** as pale yellow solid (184 mg, 75%). The Mw and Mn of P_1 were 2894 and 2504 (PDI = 1.16). ^{1}H NMR (400 MHz, DMSO-d6) δ 12.57 (s, 2H), 7.84–6.69 (m, 10H), 6.89–6.81 (m, 4H), 3.82–3.77 (m, 4H), 2.1–0.62 (m, 20H).

P-2

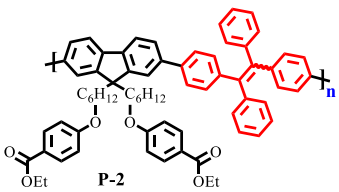

P-2

The mixture of **M-1** (86 mg, 0.146 mmol), **M-2** (120 mg, 0.146 mmol), $Pd(PPh_3)_4$ (19 mg, 0.016 mmol), and Na_2CO_3 (312 mg, 2.9 mmol) in Toluene/H_2O (8 mL: 2 mL) in a Schlenk tube was stirred at 100 °C for 72 h under the argon atmosphere. After reaction, the resulting polymers were purified by being precipitated in methanol twice. Then the solids were dried in vacuum to afford **P-2** as green solid (118 mg, 77%). ^{1}H NMR (400 MHz, $CDCl_3$) δ (ppm): 7.97–7.91 (m, 4H), 7.89–7.42 (m, 11H), 7.20–7.04 (m, 13H), 6.85–6.78 (m, 4H), 4.36–4.31 (m, 4H), 3.90–3.80 (m, 4H), 1.99–1.92 (m, 4H), 1.62–1.56 (m, 4H), 1.39–1.34 (m, 6H), 1.23–1.17 (m, 4H), 1.14–1.11 (m, 4H), 0.70–0.58 (m, 4H).

P_2

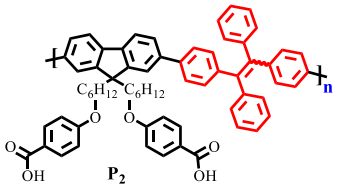

P_2

P-2 (118 mg, 0.116 mmol) and NaOH (92.4 mg, 2.31 mmol) were dissolved in 50 mL THF, and the reaction mixture was heated at 80 °C overnight. After the reaction mixture was cooled to room temperature, the solution was adjusted pH to ~2 followed by filtration. The solvent was removed under reduced pressure, and the residue was purified by being precipitated in methanol twice. Then the solids were dried in vacuum to afford **P_2** as green solid (88 mg, 60%). The Mw and Mn of **P_2** were 4817 and 3706 (PDI = 1.30). ^{1}H NMR (400 MHz, DMSO-d6) δ 12.57 (s, 2H), 7.82–6.83 (m, 32H), 3.78–3.62 (m, 4H), 2.01– 0.48(m, 20H).

In the 1H NMR of **P_1** and **P_2**, the peak of 12.57 ppm (the H of carboxylic acid) was appeared, which indicated the successful polymerization of the target polymers. Additionally, **P_1** and **P_2** showed good solubility in polar solvents, such as THF, DMSO, and DMF, due to the presence of carboxyl group.

Apparatus and characterization.

High-resolution transmission electron microscopy was performed with a JEM-2100 transmission electron microscope (JEOL Ltd., Japan). The UV-vis absorption spectra was obtained on a Shimadzu UV-3600 UV-vis-NIR photospectrometer (Shimadzu Co., Japan). The fluorescence spectra was recorded with a Hitachi F-7000 fluorescence spectrophotometer (Hitachi Ltd., Japan) equipped with a xenon lamp. The fluorescence lifetime measurement was performed on a FLS 980 spectrophotometer (Edinburgh Instruments., U.K.). The instrument is based on time-correlated single photon counting (TCSPC) with a 365 nm pulsed LED light source. For the absolute quantum yields (QY_{PL}) measurement at room temperature, the samples were placed in an optical barium sulfate coated integrating sphere (Edinburgh Instruments., U.K.) fitted in the fluorimeter sample chamber and coupled to the FLS980 spectrometer (Edinburgh Instruments., U.K.). The dynamic light scattering (DLS) and Zeta potential analysis were performed on a 90 Plus/BI-MAS equipment (Brookhaven., U.S.A.). The molecular weight was determined by gel permeation chromatography (GPC) analysis,

which was performed on a PL-GPC 50 integrated GPC (Agilent Technologies Inc., U.S.A.) equipped with refractive index detector. The THF was used as the eluent relative to polystyrene standards. And NMR spectra was recorded on a Bruker Advance 400 spectrometer (Bruker Corporation., German) at 400 MHz for ^{1}H NMR and 100 MHz for ^{13}C NMR reported as parts per million (ppm) from the internal standard tetramethylsilane (TMS).

The entire transient ECL experiment was tested by our self-built instrument. The CHI 660E electrochemical workstation was used as voltage output device. The transient ECL test was done in a self-contained blackbox and three-electrode system was placed in it and a few millimeters from the PMT (Hamamatsu, R9420, Japan) at the bottom of the cassette. The PMT received ECL signal to generate photocurrent, which was directly converted into a voltage signal through the amplifier unit (Hamamatsu, C12419, Japan) and fed into the external input channel of the oscilloscope along with the voltage and current signals recorded by the electrochemical workstation. The oscilloscope as receiving device recorded the entire transient process.

Preparation of the PNs.

The well-dispersed PNs were prepared in aqueous solution by reprecipitation method. In short, 1 mL of P_1 (130 μg/mL) or P_2 (190 μg/mL) dissolved in THF was quickly injected into 10 mL of Millipore water and under sonication for 3 min. After that, THF was removed by high purity argon stripping and then rotary evaporation under vacuum. The resulting PNs solution was filtered through a 0.22 μm pore-size filter (Millex GP, PES membrane). The as-synthesized PNs were colorless (inset of Figure S12) and transparent, and stable for months when stored at 4 °C.

It is known that the molar mass of the repeating unit of the polymer is 635 g/mol (P_1) and 965 g/mol (P_2), respectively. We could calculate the concentration of the prepared nanoparticle as:

$$\text{PNs-1:}\quad \frac{130\ \mu g/mL \times 1\ mL}{10\ mL \times 635\ g/mol} = 20\ \mu M$$

$$\text{PNs-2:}\quad \frac{190\ \mu g/mL \times 1\ mL}{10\ mL \times 965\ g/mol} = 20\ \mu M$$

Electrochemical and ECL Measurements.

Electrochemical experiments were performed on a CHI 660E electrochemical workstation (CH Instruments Inc., U.S.A.). The cyclic voltammetry (CV) for 0.5 mM polymers were studied in MeCN/Bz (1:1, v/v) mixed solvent and 0.1 M $TBAPF_6$ as the supporting electrolyte in a homemade glass cell under argon atmosphere. A conventional three-electrode system: a glassy carbon electrode (GCE from CHI Instruments Inc., Shanghai) with 3 mm diameter as the working electrode, a platinum wire as the counter electrode and a silver wire as quasi-reference electrode. Before each experiment, the working electrode was polished with 0.05 μm alumina (CHI Instruments Inc., Shanghai) for several minutes and alternating ultrasound in ethanol and aqueous solution. The counter and reference electrodes were also cleaned by rinsing in water and ethanol solution. Finally, all the electrodes were blown dry with a

stream of nitrogen. The quasi-reference electrode was separated from the electrolyte by glass tube and was calibrated against a saturated calomel electrode (SCE) by the addition of ferrocene as an internal standard at the end of each experiment, taking $E^{o}_{Fc/Fc^{+}}$ = 0.446 V vs SCE.

The ECL emission signals were recorded on MPI-E multifunctional electrochemical and chemiluminescent analytical system (Xi'an Remax Analytical Instrument Co. Ltd., China). And we used PNs modified glassy carbon electrode (PNs/GCE) as the working electrode and an Ag/AgCl electrode as the reference electrode, while the counter electrode remained unchanged. Three-electrode system were positioned a few millimeters from the PMT in a homemade blackbox. The ECL spectrum were measured with a series of different optical filters (20 nm spaced), which were placed in front of the PMT window of blackbox and the ECL intensity of corresponding wavelength filter were recorded. The ECL photographs were recorded with an Olympus DP71 cooled CCD camera (2 s exposure) and analyzed by Image-Pro Plus (IPP) 6.0 software. Apart from this, we mixed 1 mL $Ru(bpy)_3^{2+}$ (20 μM, the same concentration as the PNs-2) with 40 μL Nafion solution. The mixtures were ultrasonicated for 30 min, and then fixed on the GCE surface and measured ECL intensity under the same experimental conditions. $Ru(bpy)_3^{2+}$ is a molecule with excellent water solubility. Without surface protection, it could dissolve rapidly with dramatically decreased ECL signal intensity (Figure S17A). In order to solve this problem, we usually choose to mix it with Nafion to achieve stable emission with slight compromise of the ECL intensity (Figure S17B). And the ECL efficiency were calculated by the formula reported in previously literature and compared with the standard reference $Ru(bpy)_3^{2+}$/TPrA.

The relative ECL efficiency formula:

$$\frac{\Phi_{ECL}}{\Phi^{o}_{ECL}} = \left(\frac{I}{Q}\right) / \left(\frac{I^{o}}{Q^{o}}\right)$$

where Q and Q° are the values of consumed charges and calculated by integrating current *vs* time, I and I° are the values of total ECL intensity and calculated by integrating ECL spectrum *vs* wavelength, and ECL and °ECL are the ECL efficiency of the sample and standard ($Ru(bpy)_3^{2+}$), respectively. In this work, the °ECL value of $Ru(bpy)_3^{2+}$ was recognized as 1.